Modelling spin transfer torque and magnetoresistance in magnetic multilayers

2007 J. Phys.: Condens. Matter 19 165212

(http://iopscience.iop.org/0953-8984/19/16/165212)

IOP PUBLISHING JOURNAL OF PHYSICS: CONDENSED MATTER

J. Phys.: Condens. Matter **19** (2007) 165212 (42pp) doi:10.1088/0953-8984/19/16/165212

Modelling spin transfer torque and magnetoresistance in magnetic multilayers

A Manchon[1], N Ryzhanova[1,2], N Strelkov[1,2], A Vedyayev[1,2] and B Dieny[1]

[1] SPINTEC, URA 2512 CEA/CNRS, CEA/Grenoble, 38024 Grenoble Cedex 9, France
[2] Department of Physics, Lomonosov University, Moscow, Russia

E-mail: vedy@magn.ru

Received 16 August 2006
Published 6 April 2007
Online at stacks.iop.org/JPhysCM/19/165212

Abstract

Theoretical models of spin-dependent transport in magnetic spin-valves and tunnel junctions are presented. A general definition of current-induced spin transfer torque (STT) and interlayer exchange coupling (IEC) based on the spin density continuity principle is given. We then present an extension of the Valet and Fert model, based on the Boltzmann description of spin-dependent transport in metallic structures. This model describes STT and IEC in any kind of magnetic metallic multilayer, for any orientation of the magnetization of the ferromagnetic layers. Simulation results show that spin torque and magnetoresistance originate from the same physical effect. In a second step, we model STT and IEC in magnetic tunnel junctions with an amorphous insulator, using the non-equilibrium Keldysh technique. The general features of STT and IEC are described, showing an important asymmetry in STT bias dependence. Moreover, the influence of a layer of impurities in the barrier is investigated and shows an important enhancement of STT and IEC at resonance. Finally, we apply this model to double magnetic tunnel junctions and show that a dramatic enhancement of spin torque can be obtained when the conditions of resonance in the free layer are fulfilled.

1. Introduction

The interaction of flowing electrons with the background magnetization inside a ferromagnet has been intensively studied for the past two decades, leading to outstanding discoveries such as giant [1] and tunnelling [2] magnetoresistance. The design of metallic spin-valves (MML) [3] and magnetic tunnel junctions (MTJ) [4] has greatly improved our knowledge of magneto-electronic transport, giving rise to a new field of investigation known as 'spintronics' [5]. Its effective and potential applications in read-heads [6], RF components [7] or non-volatile memory (magnetic random access memory (MRAM)) [8] contribute greatly to its popularity in the scientific community.

One of the main exciting effects in spintronics is the reciprocal influence of a spin-polarized current on the background magnetization [9]. This phenomenon, known as 'spin transfer torque' (STT), permits the control of the magnetization in a spin-valve-based nanostructure using only the electrical current flowing through it.

The first insight into spin torque was proposed by Slonczewski in 1989, in his free-electron model of magnetic tunnel junctions [10]. In this paper, the author analysed the magnetization response to a spin-polarized electrical current and found that spin current induced a pseudo-torque on the magnetization. However, energy dissipation and current-induced heating were expected to hide the pseudo-torque effect. Fortunately, the recent development of e-beam lithographic processes allowed fabricating submicron devices (MMLs as well as MTJs) in which the applied current density can be high enough to generate such a torque (provided that the resistance–area product (RA) remains lower than 10 $\Omega\ \mu m^2$).

In 1996, Slonczewski [11] and Berger [12] showed theoretically that an electrical current flowing through a MML can induce a torque on the background magnetization generating magnetic excitations and even magnetization switching. Less than 2 years after these theoretical demonstrations, experimental data confirmed these predictions [13] and brought a number of exciting results, enriching the physics of spin-dependent transport in both magnetic metallic multilayers [14–16] and magnetic tunnel junctions [17–19]. These static and dynamic results led to a large number of theoretical works [20–28] and micromagnetic simulations [29, 30].

In this paper we propose a general study of spin torque and magnetoresistance in magnetic metallic multilayers and tunnel junctions, in order to reveal the specific features of spin-dependent transport in such structures. In section 2, we give the definition of spin transfer torque based on quantum mechanical considerations and we present a general overview of the different theories of spin transfer torque in MMLs and MTJs. Section 3 deals with the modelling of spin torque inside MML, using a Boltzmann-based description of the diffusive transport extended to any kind of multilayer. Section 4 presents a study of spin torque and current-driven exchange coupling in MTJ with an amorphous barrier, based on the Keldysh non-equilibrium technique. The influence of a layer of impurities inserted within the insulating barrier is investigated. In section 5 the previous theory is applied to double magnetic tunnel junctions (DMTJ) and the influence of quantum states inside the central free layer is investigated.

2. General overview

2.1. Continuity principle of spin density

The fundamental physics of spin transfer torque is contained in the continuity principle of spin density which allows the transfer of itinerant-electron spins to the background magnetization of a ferromagnet. We consider the s–d model in which s-electrons are itinerant and d-electrons are localized and give rise to the local magnetization of the ferromagnet. This model applies to the electron structures of ferromagnetic electrodes whose compositions lie on the negative slope side of the Slater–Néel–Pauling curve (Ni, Co, NiFe, CoFe). Consider an arbitrary two-dimensional Hartree–Fock wavefunction $\Psi(\mathbf{r}, t)$. The two dimensions refer to up ($\uparrow$) and down ($\downarrow$) spin components of the Hartree–Fock wavefunction. Then, the local spin density $\overrightarrow{s}$ at the location $\mathbf{r}$ and time t is

$$\overrightarrow{s}(\mathbf{r}, t) = \Psi^*(\mathbf{r}, t)\frac{\hbar}{2}\overrightarrow{\sigma}\,\Psi(\mathbf{r}, t) \tag{2.1}$$

where $\overrightarrow{\sigma}$ is the Pauli matrix. The time variation of spin density is then:

$$\frac{\mathrm{d}}{\mathrm{d}t}\overrightarrow{s}(\mathbf{r}, t) = \frac{\hbar}{2}\left\{\frac{\mathrm{d}}{\mathrm{d}t}\Psi^*\overrightarrow{\sigma}\,\Psi + \Psi^*\overrightarrow{\sigma}\,\frac{\mathrm{d}}{\mathrm{d}t}\Psi\right\}. \tag{2.2}$$

Furthermore, the time-dependent Schrödinger equation gives $\frac{\mathrm{d}}{\mathrm{d}t}\Psi(\mathbf{r},t) = -\frac{\mathrm{i}}{\hbar}H\Psi(\mathbf{r},t)$, where H is the Hamiltonian of the system. Substituting this equation in (2.2) we get:

$$\frac{\mathrm{d}}{\mathrm{d}t}\vec{s}\,(\mathbf{r},t) = \frac{1}{2\mathrm{i}}\{\Psi^*\vec{\sigma}\,H\Psi - (H\Psi)^*\vec{\sigma}\,\Psi\}. \tag{2.3}$$

In the non-relativistic limit, the Hamiltonian for itinerant s-electrons in a ferromagnet is written:

$$H = \frac{p^2}{2m} - U(\mathbf{r}) - J_{\mathrm{sd}}(\vec{\sigma}\cdot\vec{S_{\mathrm{d}}}) \tag{2.4}$$

where the first and second terms are the kinetic and potential energies, while the third term is the s–d exchange-energy, with $\vec{S_{\mathrm{d}}}$ the local magnetization due to d-electrons and J_{sd} is the exchange constant. Equation (2.3) then reduces to [31]:

$$\frac{\mathrm{d}}{\mathrm{d}t}\vec{s}\,(\mathbf{r},t) = -\nabla\mathbf{J}_s(\mathbf{r},t) + \frac{J_{\mathrm{sd}}}{\hbar}\vec{S_{\mathrm{d}}}\times\vec{s}\,(\mathbf{r},t) \tag{2.5}$$

where $\mathbf{J}_s = \mathbf{J}_\uparrow - \mathbf{J}_\downarrow$ is the spin current in spin space and $\mathbf{J}_{\uparrow(\downarrow)}$ is the up- (down-)spin electrical current. In steady state, (2.5) reduces to [26]:

$$\nabla\mathbf{J}_s(\mathbf{r},t) = \frac{J_{\mathrm{sd}}}{\hbar}\vec{S_{\mathrm{d}}}\times\vec{s}\,(\mathbf{r},t). \tag{2.6}$$

Furthermore, we can introduce the spin density variation, given by (2.5), in the macroscopic equation of motion of total electron magnetizations, known as the Landau–Lifshitz–Gilbert (LLG) equation:

$$\frac{\mathrm{d}\vec{M}}{\mathrm{d}t} = \alpha\vec{M}\times\frac{\mathrm{d}\vec{M}}{\mathrm{d}t} - \gamma\left(\vec{M}\times\vec{H_{\mathrm{eff}}} + \frac{J_{\mathrm{sd}}}{\hbar\mu_{\mathrm{B}}}\vec{M}\times\vec{s}\,(\mathbf{r},t)\right) \tag{2.7}$$

where $\vec{M}$ is the background magnetization of the ferromagnet, γ is the gyromagnetic ratio, α is the Gilbert damping coefficient, μ_{B} is the Bohr magneton and $\vec{H_{\mathrm{eff}}}$ is the usual effective field.

This fundamental statement is very important for understanding the origin of spin transfer torque. It shows the equivalence between spin transfer torque and spin current, and implies that calculating currents in non-collinear structures is necessary and sufficient to determine spin torque.

2.2. Building transverse spin current

Different models for currents and torques in multilayered structures, MMLs and MTJs, have been proposed. When reading the very important theoretical literature about spin transfer torque (see [30] for references), one can distinguish between two main approaches, depending on the transport mechanism considered, ballistic or diffusive.

2.2.1. Ballistic spin torque. In his first theories, applied to MTJ [10] and MML [11], Slonczewski considered a quantum-mechanical system in the pure ballistic limit, i.e. neglecting the electron diffusion and spin-flip. This was fully justified in the case of MTJ but was not appropriate for metallic spin-valves in which bulk and interfacial spin-diffusion dominate [1].

In this framework, electron scattering and spin accumulation are neglected, as well as the distinction between electric and electrochemical potentials [32]. The first model applied to MML led to an angular dependence of spin torque:

$$\vec{T} = \frac{I}{e}\frac{1}{-4+(1+P)^3(3+\cos\theta)/4P^{3/2}}\cdot\vec{m}\times(\vec{m}\times\vec{p}). \tag{2.8}$$

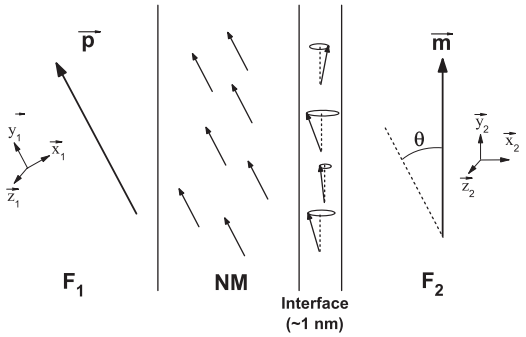

Figure 1. Schematics of the mechanism of spin transfer torque in a metallic trilayer. Polarized electrons flowing from left to right precess around the right layer magnetization with different frequencies due to their different incident angles at the interface. This results in ballistic interference yielding an oscillation and damping of spin torque near the interface (typically 1 nm).

Here, $\overrightarrow{T}$ is the macroscopic torque vector, I is the electrical current, e is the electron charge, P is the current polarization and $\overrightarrow{m}$ and $\overrightarrow{p}$ are unitary vectors collinear to the magnetization of the free and pinned layer, respectively (see figure 1). Applied to a MTJ, this model leads to a simple sine type angular dependence [21], as found in section 4.

Other ballistic models applied to MTJ have been proposed [33], but the difficulty of performing such experiments led theoreticians to focus on diffusive models in order to explain the numerous experimental results obtained in MML.

2.2.2. Diffusive spin torque. In metallic multilayers, electron spin-diffusion plays a dominant role leading to spin accumulation, which is neglected in the ballistic approach. This spin accumulation is proportional to the difference of chemical potentials $\Delta\mu$ for spin-up and spin-down electrons and $\Delta\mu \approx E \cdot l_{sd}$, where l_{sd} is the spin-diffusion length of the material and E the electric field applied to the structure. Consequently, in metallic multilayers, spatial variation of spin accumulation cannot be neglected, which is not the case in magnetic tunnel junctions, where the drop of potential mainly occurs in the barrier so that $\Delta\mu$ can be neglected in the outer electrodes.

Three main theories, generally equivalent, have been proposed to model spin transfer torque. The more generally used theory is the Valet and Fert Boltzmann-like approach [32]. The Boltzmann equation describes the evolution of electronic states near the Fermi level. In this theory, electronic transport is described in terms of currents and electrochemical potentials and both bulk and interfacial spin scattering contribute to the construction of spin polarization and spin accumulation [23]. Another approach, which is equivalent to the Boltzmann description, is the drift-diffusion model employed by Stiles *et al* [22, 34].

Slonczewski proposed a circuit model in which the spacer resistivity and spin-diffusion are neglected [20, 35]. This model has been generalized to any kind of MML, including interfacial spin-flip [36]. The main difference between circuit theory and the Boltzmann approach is that circuit theory neglects the spatial variation of spin accumulation. Nevertheless, Xiao *et al* [34] showed that this circuit theory could be generalized to systems where spin accumulation is spatially varying and that spin torque results derived from circuit theory were essentially confirmed by solving the Boltzmann equation in any kind of structure.

In a third approach, Zhang *et al* [24] showed that the first spin transfer torque predicted by Slonczewski [11] should be completed by a current-driven interlayer exchange coupling (IEC),

generated by transverse spin accumulation. The relative amplitude of IEC compared to STT is not yet theoretically stated, however. Recently Kubota *et al* [37] estimated the IEC amplitude to be of the order of 10% of the amplitude of spin torque in a MgO-based MTJ. In the rest of this paper we propose a study of IEC together with STT.

2.2.3. Further theories. To conclude this overview of spin torque theories, we underline the fact that other theoreticians have worked on current-induced spin-wave emission [25] to explain the high frequency magnetic excitations found in dynamic experimental investigations.

Furthermore, the reciprocal effect of magnetic excitations generating spin current and vice versa (also called spin pumping) has been studied by Tsernovnyak *et al* [28]. We will not develop these approaches which are outside the scope of this work, and invite the reader to refer to the references given at the end of this paper.

Finally, we note an interesting recent theoretical work predicting spin transfer in antiferromagnets [38]. Some preliminary experimental results seem to confirm the existence of such a phenomenon [61], and further investigations are expected.

3. Spin torque in magnetic metallic multilayers

3.1. Introduction

The detailed semi-classical theory of spin-dependent perpendicular-to-plane (CPP) transport in multilayered magnetic structures based on the Boltzmann equation was developed in [32] taking into account both bulk and interfacial spin-dependent scattering. In this model it is emphasized that when the thickness of the layers is comparable to or larger than spin-diffusion length, the transport properties of different spin channels cannot be considered as independent and spin-flip processes have to be taken into account. The model proposed in [32] is restricted to the structures with collinear configuration of magnetization in the magnetic layers. This approach was then extended to structures with non-collinear magnetic configuration [24, 39]. Calculation on the basis of this model for a three-layered structure, thick magnetic layer/non-magnetic layer/tilted thin magnetic layer (see figure 1), has shown that STT is governed by the spin-dependent transport parameters of the thick layer [40] which creates a polarized spin current, the spin-dependent bulk and interfacial scattering, and the resistivity and spin-diffusion length.

The formalism developed in [32, 24, 39] was applied only to particular types of structures, such as single interface or MML with an infinite number of repeats of the same bilayer. Later this model was generalized to any multilayered pillar structure with collinear magnetic configuration [41]. In addition to [32] the scattering at lateral edges of submicron multilayered pillar was included in the calculation scheme which can be viewed as a current-in-plane effect intruding in CPP transport. A universal code for numerical calculation of spin-dependent current and CPP-GMR was developed.

This section presents the further development of all these models for the calculation of CPP-GMR and spin torque for any multilayered structure and magnetic configuration. The diffuse electron and spin transport including spin-flip processes was considered on the basis of the diffusion equation. Following [12, 24] we took into account the four-component character of the current consisting of charge current and spin current with one component parallel to the magnetization of the layer considered and two transverse components with the corresponding accumulation effects. The same asymmetry parameters as in the theory of Levy *et al* are involved in the consideration presented here, but in comparison with [39], we also kept the term responsible for an additional current proportional to the gradient of non-equilibrium electron

concentration as well as an additional source of spin accumulation associated with the spin-dependent interfacial resistance. The created code can also be used for calculating the CPP-GMR and STT in pillar multilayered structures in the framework of the same model, as in [41].

3.2. Diffusive model

The calculation of CPP spin-dependent current and spin torque is based on the diffusion equation and equation of motion for the spin accumulation, as was done in the Valet–Fert model [32] and similar models for a MML structure with a non-collinear configuration of magnetization [12, 24]. Following [12, 24] and a generalized form of [11] for any multilayered pillar structure [39], we start from the following expressions for the charge j_n^e and spin $\overrightarrow{j_n^m}$ components of the current:

$$j_n^e = \frac{E_x}{\rho_n} - D_{0n}\frac{\partial n_n^0}{\partial x} - D_{0n}\beta'\left(M_n^x\frac{\partial m_n^x}{\partial x} + M_n^y\frac{\partial m_n^y}{\partial x} + M_n^z\frac{\partial m_n^z}{\partial x}\right) \tag{3.1a}$$

$$\overrightarrow{j_n^m} = \frac{\beta_n E_x \overrightarrow{M_n}}{\rho_n} - D_{0n}\beta'\overrightarrow{M_n}\frac{\partial n_n^0}{\partial x} - D_{0n}\frac{\partial \overrightarrow{m_n}}{\partial x}. \tag{3.1b}$$

In (3.1*a*) and (3.1*b*), superscripts x, y and z mean components in spin space, E_x is the external electric field directed perpendicular to the interfaces of the multilayered structure, n is the layer index and ρ_n and D_{0n} are the resistance and diffusion coefficients, respectively. In the chosen geometry, the x-axis is perpendicular to the plane of the layers. $\overrightarrow{M_n}$ is the spontaneous local magnetization, homogeneous inside every magnetic layer but changing from layer to layer, and we choose $\overrightarrow{M_n} = \left(M_n^x, 0, M_n^z\right) = (\sin\Theta_n, 0, \cos\Theta_n)$. Both resistance and diffusion coefficients are spin-dependent:

$$1/\rho_n^{\uparrow(\downarrow)} = (1 \pm \beta_n)/2\rho_n$$
$$D_n^{\uparrow(\downarrow)} = D_{0n}\left(1 \pm \beta_n'\right).$$

Non-equilibrium electron concentration n_n (charge accumulation) is connected with non-equilibrium magnetization $\overrightarrow{m_n}$ (spin accumulation) by the relations:

$$n_n^{\uparrow} + n_n^{\downarrow} = n_n^0$$
$$n_n^{\uparrow} - n_n^{\downarrow} = |\overrightarrow{m_n}|.$$

The coefficients of asymmetry β_n, β_n' are not independent and are related via the asymmetry coefficient for the electron with up (down) spins density of states: $N_n^{\uparrow(\downarrow)} = \frac{1}{2}N_{n0}(1 \pm \delta_n)$. So, from the Einstein relation $1/\rho_n = e^2 N_n(E_F) D_n$, it follows that:

$$\begin{aligned} D_{0n} &= \frac{1 - \beta_n\delta_n}{e^2\rho_n N_{n0}(1 - \delta_n^2)} \\ D_{0n}\beta_n' &= \frac{\beta_n - \delta_n}{e^2\rho_n N_{n0}(1 - \delta_n^2)} \\ \beta_n' &= \frac{\beta_n - \delta_n}{1 - \beta_n\delta_n}. \end{aligned} \tag{3.2}$$

The currents (3.1*a*) and (3.1*b*) have to be inserted into the conditions for non-divergent current components:

$$\begin{aligned} &\frac{\partial j_n^e}{\partial x} = 0 \\ &\frac{\partial \overrightarrow{j_n^m}}{\partial x} + \frac{J}{\hbar}[\overrightarrow{m_n} \times \overrightarrow{M_n}] + \frac{\overrightarrow{m_n}}{\tau_{nsf}} = 0 \end{aligned} \tag{3.3}$$

where J is the parameter of s–d exchange interaction and τ_{nsf} is the spin-flip relaxation time. At this stage, we should make a comment about (3.3). Recently, Levy *et al* proposed a Boltzmann-based model of spin torque in which they introduced a term of spin precession around the background magnetization. As a matter of fact, in the ballistic regime (see figure 1), one can show that the transverse spin accumulation decays within a length of $2\pi/(k_F^{\uparrow} - k_F^{\downarrow})$. In figure 10, we show the oscillation and damping of spin torque proportional to the transverse spin accumulation in the case of a magnetic tunnel junction. The oscillation has a period of $2\pi/(k_F^{\uparrow} - k_F^{\downarrow}) \approx 12$ Å. However, some authors rejected this term, arguing that in the diffusive regime it is not possible to consider physical processes which take place in a distance smaller than the mean free path λ of the electron (the Valet and Fert Boltzmann model applies to structures where $\lambda \ll l_{sf}$). This is the reason why some authors consider that spin transfer torque occurs at the interface. In this case, the spin transfer is taken as a boundary condition and spin torque is calculated from the interfacial discontinuity of the spin accumulation [42]. Indeed, for usual ferromagnets, the spin precession time τ, inversely proportional to the exchange splitting energy J_{sd}, is of the order of $10^{-15}/J_{sd}$ s. For strong ferromagnets, with high exchange energy (of the order of 1 eV), the precession time is short compared to the collision time $\tau_e = \lambda/v_F \approx 10^{-14}$, where v_F is the Fermi velocity. Consequently, in such a ferromagnet, spin accumulation vanishes within a region where the transport regime is ballistic. On the other hand, considering weak ferromagnets, the spin accumulation decreases over a much larger distance where the regime is diffusive. To be convenient, our model should be restricted to weak ferromagnetic multilayers. The case of strong ferromagnetic layers should combine both ballistic and diffusive approaches, depending on the spin accumulation decay length. This combined approach is under investigation.

Let us come back to our calculation. Using (3.1*a*), (3.1*b*) and (3.3) we can remove the unknown n_n^0 from the system:

$$\frac{\partial^2 n_n^0}{\partial x^2} = -\beta_n' \left(\sin\Theta_n \frac{\partial^2 m_n^x}{\partial x^2} + \cos\Theta_n \frac{\partial^2 m_n^z}{\partial x^2} \right). \tag{3.4}$$

The system can then be written down for $\overrightarrow{m_n}$:

$$\begin{aligned}
&D_{0n}\frac{\partial^2 m_n^x}{\partial x^2}\left(\beta_n'^2 \sin^2\Theta_n - 1\right) + \frac{J}{\hbar} m_n^y \cos\Theta_n + \frac{m_n^x}{\tau_{nsf}} + \frac{1}{2} D_{0n}\beta_n'^2 \sin 2\Theta_n \frac{\partial^2 m_n^z}{\partial x^2} = 0 \\
&-D_{0n}\frac{\partial^2 m_n^y}{\partial x^2} + \frac{J}{\hbar}\left(m_n^z \cos\Theta_n - m_n^x \sin\Theta_n\right) + \frac{m_n^y}{\tau_{nsf}} = 0 \\
&\frac{1}{2} D_{0n}\beta_n'^2 \sin 2\Theta_n \frac{\partial^2 m_n^x}{\partial x^2} - \frac{J}{\hbar} m_n^y \sin\Theta_n + \frac{m_n^z}{\tau_{nsf}} + \frac{1-\beta_n\delta_n}{\rho_n}\left(\beta_n'^2 \cos^2\Theta_n - 1\right)\frac{\partial^2 m_n^z}{\partial x^2} = 0.
\end{aligned} \tag{3.5}$$

To find $\overrightarrow{m_n}$ we perform a unitary transformation of the matrix of coefficients $\hat{m}$ of the system (3.5), $\tilde{\hat{m}} = \hat{R}^{-1}\hat{m}\hat{R}$, where $\hat{R}$ is the rotation matrix:

$$\hat{R} = \begin{bmatrix} \cos\Theta_n & 0 & \sin\Theta_n \\ 0 & 1 & 0 \\ -\sin\Theta_n & 0 & \cos\Theta_n \end{bmatrix}. \tag{3.6}$$

In the local system of coordinates, (3.5) has a very simple form:

$$\begin{aligned}
&-D_{0n}\frac{\partial^2 m_n^x}{\partial x^2} + \frac{m_n^x}{\tau_{nsf}} + \frac{J}{\hbar} m_n^y = 0 \\
&-D_{0n}\frac{\partial^2 m_n^y}{\partial x^2} + \frac{m_n^y}{\tau_{nsf}} - \frac{J}{\hbar} m_n^x = 0 \\
&D_{0n}\frac{\partial^2 m_n^z}{\partial x^2}\left(\beta_n'^2 - 1\right) + \frac{m_n^z}{\tau_{nsf}} = 0.
\end{aligned} \tag{3.7}$$

The solution of (3.7) is:

$$\begin{aligned} m_n'^x &= c_{1n}\mathrm{e}^{k_{1n}(x-x_n)} + c_{2n}\mathrm{e}^{-k_{1n}(x-x_n)} + c_{3n}\mathrm{e}^{\mathrm{i}k_{2n}(x-x_n)} + c_{4n}\mathrm{e}^{k_{2n}(x-x_n)} \\ m_n'^y &= \mathrm{i}\left(c_{1n}\mathrm{e}^{k_{1n}(x-x_n)} + c_{2n}\mathrm{e}^{-k_{1n}(x-x_n)} - c_{3n}\mathrm{e}^{k_{2n}(x-x_n)} - c_{4n}\mathrm{e}^{k_{2n}(x-x_n)}\right) \\ m_n'^z &= c_{5n}\mathrm{e}^{k_{3n}(x-x_n)} + c_{6n}\mathrm{e}^{-k_{3n}(x-x_n)} \end{aligned} \tag{3.8}$$

where

$$\begin{aligned} k_{n1,2} &= \sqrt{\frac{1}{\lambda_{n\mathrm{sf}}^2} \pm \mathrm{i}\frac{1}{\lambda_{nJ}^2}} \\ k_{n3} &= \sqrt{\frac{1}{\lambda_{n\mathrm{sf}}^2\left(1-\beta_n'^2\right)}} \\ \lambda_{n\mathrm{sf}}^2 &= \tau_{n\mathrm{sf}} D_{0n} \\ \lambda_{nJ} &= \frac{\hbar}{J} D_{0n} \end{aligned}$$

and x_n is the coordinate of the interface between layers $n-1$ and n. Going back to the former system of coordinates, we have:

$$\begin{aligned} m_n^x &= \cos\Theta_n m_n'^x + \sin\Theta_n m_n'^z \\ m_n^y &= m_n'^y \\ m_n^z &= -\sin\Theta_n m_n'^x + \cos\Theta_n m_n'^z \end{aligned} \tag{3.9}$$

and then after a double integration of (3.4):

$$n_n^0 = -\beta_n'\left(c_{5n}\mathrm{e}^{k_{3n}(x-x_n)} + c_{6n}\mathrm{e}^{-k_{3n}(x-x_n)}\right) + c_{7n} + c_{8n}x. \tag{3.10}$$

Next, all the coefficients $c_{1n}\ldots c_{8n}$ have to be found. Inserting (3.9) and (3.10) in (3.1*a*) and (3.1*b*) and writing down the conditions of equality of currents in the layers n and $n+1$, four recurrent equations for the coefficients c_{in} are obtained. For example:

$$j_n^e = \frac{E_x}{\rho_n} - D_{0n}c_{8n} = \frac{E_x}{\rho_{n+1}} - D_{0n+1}c_{8n+1}. \tag{3.11}$$

One can see from (3.11) that the set of equations for the coefficients c_{8n} may be solved independently and all these coefficients will be expressed through c_{80}.

To obtain additional equations to complete the system we use the continuity of the current in the bulk of each layer and through the interfaces. These currents can be expressed through the difference of chemical potentials in adjacent layers $\mu_n^{\uparrow(\downarrow)} = \mu_n \pm |\Delta\vec{\mu_n}|$:

$$\begin{aligned} \mu_n &= \frac{n_n^0 - \delta_n\vec{M_n}\cdot\vec{m_n}}{N_{0n}\left(1-\delta_n^2\right)} \\ \overrightarrow{\Delta\mu_n} &= \frac{\vec{m_n} - \delta_n n_n^0\vec{M_n}}{N_{0n}\left(1-\delta_n^2\right)}. \end{aligned} \tag{3.12}$$

The interfacial currents are:

$$\begin{aligned} \tilde{j_n^e} &= \frac{\mu_n - \mu_{n+1}}{r_n} + \frac{\vec{\gamma_n}}{r_n}.\left(\overrightarrow{\Delta\mu_n} - \overrightarrow{\Delta\mu_{n+1}}\right) \\ \vec{\tilde{j_n^m}} &= \frac{\overrightarrow{\Delta\mu_n} - \overrightarrow{\Delta\mu_{n+1}}}{r_n} + \frac{\vec{\gamma_n}}{r_n}(\mu_n - \mu_{n+1}) \end{aligned} \tag{3.13}$$

where

$$\begin{aligned} \vec{\gamma_n} &= \gamma_n\left[\overrightarrow{M_{n+1}}\beta_{n+1} + \vec{M_n}\beta_n\right]/\left[\beta_n + \beta_{n+1}\right] \\ r_n^{\uparrow(\downarrow)} &= r_n\left(1 \mp |\vec{\gamma_n}|\right) \end{aligned}$$

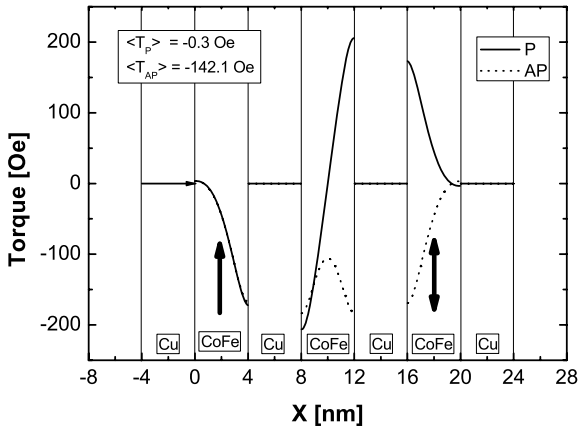

Figure 2. Dependence of the spin torque on the coordinate X, perpendicular to the planes of the layers for the values of parameters depicted in table 1. Spin torque is given for parallel (solid line) and antiparallel (dotted line) configurations of the pinned layers. $\langle T \rangle$ is the spin torque in the free layer, averaged over its thickness.

Table 1. Material parameters used in the simulations. The interfacial resistance (r) and interfacial spin asymmetry (γ) are introduced for modelling CoFe/Cu interfaces.

	ρ ($\mu\Omega$ cm)	β	δ	r (mΩ μm^2)	γ	λ_{sf} (nm)	λ_J (nm)
CoFe	19	0.55	0.75	40	0.7	15	1
Cu	5	0	0	40	0.7	100	

r_n is the interfacial resistance between the layers n and $n+1$. After some algebra, the resulting system has the form:

$$\hat{A}_n \hat{C_{n+1}} = \hat{B}_n \hat{C}_n + \hat{R}_n \tag{3.14}$$

where $\hat{C_{n+1}} = [c_{1n} \dots c_{7n}]^{\mathrm{T}}$ and $\hat{A}_n$, $\hat{B}_n$ are 7×7 matrices, the explicit form of which is given in appendix A. To close the system we choose cyclic boundary conditions and take the constant c_{70} equal to zero. In addition the spin-dependent reflection from the border of the pillar is taken into account in the same model as in [39]. After that, for any multilayered stack and for arbitrary distribution of magnetizations, the system of equations (3.14) can be solved and the electrical current, CPP-GMR and spin torque proportional to the m_n^y component of the non-equilibrium magnetization can be found. A numerical code was created to this end, and we discuss some of these results below.

3.3. Results and discussion

To illustrate the dependence of the torque on the parameters of the multilayered spin-valve we choose the system Cu/$CoFe_1$/Cu/$CoFe_2$/Cu/$CoFe_3$/Cu where $CoFe_{1,3}$ are pinned layers and $CoFe_2$ is a free layer. All parameters of the system are tabulated in table 1. In figure 2, we plot the dependence of spin torque on the coordinate X perpendicular to the plane (Y, Z) of the layers. We considered that the magnetizations of all the three ferromagnetic layers are in one plane, the magnetizations of the pinned layers are collinear (parallel or antiparallel to the Z-axis) and the magnetization of the free layer has an angle $\Theta = 90^\circ$ with the Z-axis. The resulting torque lies in the YZ plane. Figure 2, presenting spin torque as a function of the

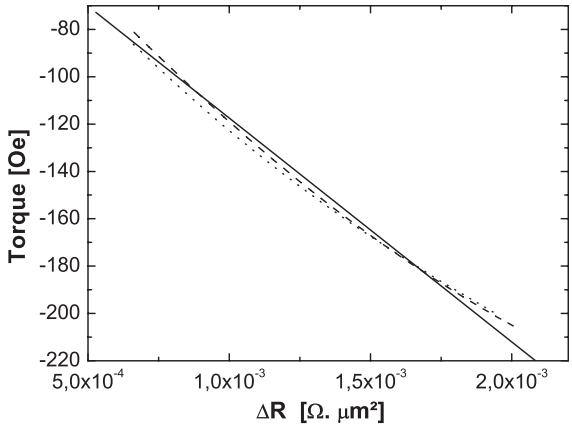

Figure 3. The dependence of spin torque in a free layer for the system $Cu/CoFe_1/Cu/CoFe_2/Cu$ versus absolute magnetoresistance ΔR, when varying the thickness t_1 (dashed line) or the bulk spin asymmetry β_1 (dotted line) of the first layer.

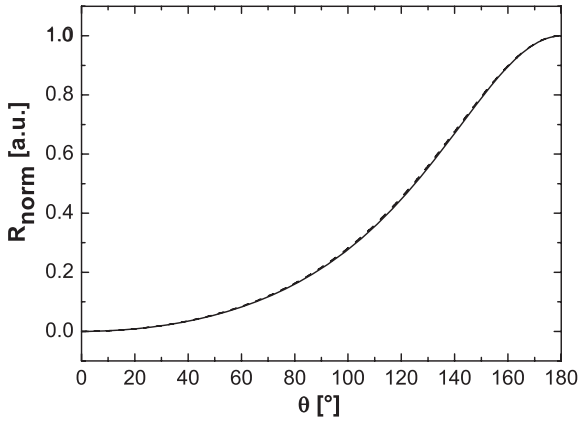

Figure 4. Normalized resistance for the system $Cu/CoFe_1/Cu/CoFe_2/Cu$ versus the angle between magnetizations of the two ferromagnetic layers (dashed line). The solid line is a fit with the phenomenological formula $R^{\mathrm{norm}} = [1 - \cos^2 \frac{\Theta}{2}]/\left[1 + \chi \cos^2 \frac{\Theta}{2}\right]$ with $\chi = 2.71$.

location along the structure, shows that the value of the torque acting on the free layer and averaged over the thickness of this layer is greatly enhanced in the antiparallel orientation of magnetizations of the pinned layers [59].

Now it is interesting to investigate the connection between spin torque and absolute magnetoresistance. So in the system $Cu/CoFe_1/Cu/CoFe_2/Cu$ we changed the values of the thickness of the first ferromagnetic layer and spin asymmetry parameters β_1 to calculate spin torque in the free layer and $\Delta R = R(\pi) - R(0)$. The plot in coordinates T, ΔR is presented in figure 3 (varying the thickness of $CoFe_1$ (dashed line) or the bulk spin asymmetry β_1 (dotted line)). These dependences almost coincide with a straight line (solid line).

In the system $Cu/CoFe_1/Cu/CoFe_2/Cu$, we investigated the dependence of the torque acting on the layer $CoFe_2$ and of the normalized resistance $R^{\mathrm{norm}}(\Theta) = [R(\Theta) - R(0)]\,/\,[R(\pi) - R(0)]$ on the angle Θ between the magnetizations of the layers $CoFe_1$ and $CoFe_2$. The results are presented in figures 4 and 5. We found that $R^{\mathrm{norm}}(\Theta)$ is

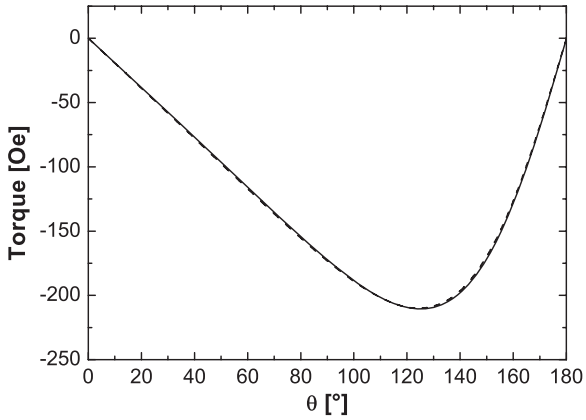

Figure 5. Torque on the free layer magnetization in the system Cu/$CoFe_1$/Cu/$CoFe_2$/Cu versus the angle between magnetizations of the two ferromagnetic layers (dashed line). The solid line is a fit with the phenomenological formula $T^{\text{norm}} = T^* \sin\Theta / \left[1 + \chi \cos^2 \frac{\Theta}{2}\right]$ with $\chi = 2.71$ and $T^* = -405$ Oe.

described by the phenomenological expression $R^{\text{norm}}(\Theta) = \left[1 - \cos^2 \frac{\Theta}{2}\right] / \left[1 + \chi \cos^2 \frac{\Theta}{2}\right]$, where $\chi = 2.71$. The dependence of torque $T^{\text{norm}}(\Theta)/T^*$ was found to be described as $T^{\text{norm}}(\Theta)/T^* = \sin\Theta / \left[1 + \chi \cos^2 \frac{\Theta}{2}\right]$ with the same value of χ. Our conclusion is that GMR and torque have the same origin. We have to note that our value of $\chi = 2.71$ is much closer to the experimentally observed $\chi = 1.17$ for the system Py(t)/Cu(20 nm)/Py(t) [62] than χ estimated in the theory [39] for the infinitely thick Co layer.

4. Spin torque in magnetic tunnel junctions

4.1. Introduction

Spin-dependent transport in magnetic tunnel junctions presents significant differences from metallic multilayers. Tunnelling transport is mainly ballistic (tunnel conductances essentially depend on the interfacial densities of states), whereas transport in metallic multilayers is most often diffusive. Since the first magnetoresistive effect observed in MTJ by Julliére [43], tremendous progresses in the preparation and understanding of the properties of these systems were achieved. Tunnel magnetoresistance amplitudes (TMR) as high as 400% are now measured at room temperature. Understanding spin torque in MTJs is of both fundamental interest and a great challenge for MRAM applications. Spin torque has been previously studied in low RA (resistance–area product) amorphous AlO_x-based MTJs [17, 18] and is under investigation in crystalline MgO-based MTJs [37]. We propose here a free-electron model based on the non-equilibrium Keldysh formalism [52] which is suitable for amorphous types of barriers (AlO_x, SiO_x) in which tunnelling of s-like electrons is dominant.

Although many theories have been proposed to explain tunnel magnetoresistance in magnetic tunnel junctions, with amorphous [43, 10, 4, 45] or crystalline barriers [46, 47], with or without impurities [48–50], only very few models have addressed the spin transfer torque in such structures [21, 51, 63, 64]. The work carried out by Kalitsov *et al* [51] proposed a first approach to spin torque in a perfect magnetic tunnel junction with an amorphous barrier, using the Keldysh formalism. The authors showed the equivalence of calculating spin torque from the point of view of spin current divergence on the one hand and from the point of view of

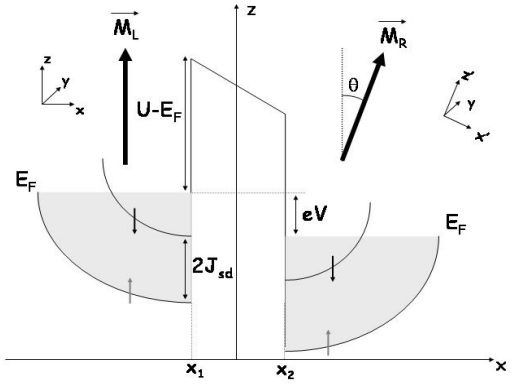

Figure 6. Schematics of a magnetic tunnel junction composed of two semi-infinite ferromagnetic electrodes separated by an amorphous barrier located between x_1 and x_2. The figure shows the split conduction bands for up- (grey arrow) and down-spins (black arrow) in the case of a parallel configuration.

the out-of-equilibrium magnetization on the other hand (see (2.5)). The model developed here is based on the same non-equilibrium technique but presents wider studies of spin torque and TMR in clean MTJs. The influence of resonant states on TMR, STT and IEC when inserting a layer of impurities within the barrier is also studied.

Our approach presents two main differences compared to Slonczewski's model [21]: first, torques are calculated from the out-of-equilibrium magnetization, which allows to directly estimate the current-driven exchange coupling ('out-of-plane torque' $T_{R\perp}$ in [21]), which is more complicated to obtain in Bardeen's Transfer Matrix formalism. Then, whereas [21] is restricted to tunnelling electrons located at the Fermi energy, we consider the contribution of all the electrons below the Fermi level. This second point will be important when considering impurities in the barrier. Most of the results presented here are consistent with the study of Theodonis *et al* [63], in which the authors used a tight-binding approach of tunnelling transport.

4.2. Theoretical framework

4.2.1. MTJ without impurities. We consider a magnetic tunnel junction composed of $F_L/I/F_R$, where $F_{L(R)}$ is the semi-infinite left (right) ferromagnetic electrode and I is a non-magnetic amorphous insulator, such as Al_2O_3. The magnetizations $\overrightarrow{M_L}$ and $\overrightarrow{M_R}$ of F_L and F_R respectively, have an angle $\theta = \cos^{-1}\left[\overrightarrow{M_L}\cdot\overrightarrow{M_R}\right]$ between them. We attribute the spin-space coordinate system (x, y, z) and (x', y, z') to the left and right ferromagnets, respectively, where z and z' are the quantization axes and x is perpendicular to the plane of the layers (see figure 6).

The current-induced effective local magnetization (spin accumulation) in F_L is denoted $\overrightarrow{m} = (m_x, m_y, m_z)$, where the transverse components are $m_x = \langle\sigma^x\rangle$ and $m_y = \langle\sigma^y\rangle$. σ^i are the Pauli spin matrices and $\langle\ \rangle$ denotes the average over orbital states and spin states, i.e. the average over electrons of energy E, transverse momentum $\overrightarrow{\kappa}$ and spin states s. The transverse effective local magnetization in the left ferromagnet is then given by $\langle\sigma_+\rangle = \langle\sigma^x + \mathrm{i}\sigma^y\rangle$. Thus $\langle\sigma^x\rangle$ is oriented along the x-axis and induces the current-driven exchange-coupling torque, whereas $\langle\sigma^y\rangle$ is oriented along the y-axis and induces the current-induced spin transfer torque. In other words, STT is given by the imaginary part of $\langle\sigma_+\rangle$, while IEC is given by its real part:

$$m_x + \mathrm{i}m_y = \langle\sigma^+\rangle = \left\langle \begin{pmatrix} \Psi^\uparrow & \Psi^\downarrow \end{pmatrix} \begin{pmatrix} 0 & 2 \\ 0 & 0 \end{pmatrix} \begin{pmatrix} \Psi^{*\uparrow} \\ \Psi^{*\downarrow} \end{pmatrix} \right\rangle = 2\langle\Psi^\uparrow\Psi^{*\downarrow}\rangle \qquad (4.1)$$

where $\Psi = (\Psi_\uparrow, \Psi_\downarrow)$ is the Hartree–Fock spinor wavefunction. In our model, no diffusion is considered in the ferromagnetic electrodes and spin torque originates only from ballistic mechanism associated with interferences between direct tunnelling and reflected polarized electrons in the ferromagnets. Considering spin-flip within the electrodes is expected to introduce a faster damping of spin torque within the electrodes but will not alter fundamentally the results discussed in this section. As discussed in section 3, formally, this model is restricted to MTJs with electrodes thinner than their mean free path λ. To determine the spin-up and spin-down components of the Hartree–Fock wavefunction $\Psi = (\Psi^\uparrow, \Psi^\downarrow)$, we use the non-equilibrium Keldysh formalism [52, 53]. In the Keldysh formalism, the right-hand-side of (4.1) corresponds to the Keldysh Green function $G^{-+}_{\uparrow\downarrow}$, which is written as:

$$G^{-+}_{\uparrow\downarrow}(\mathbf{r}, t, \mathbf{r}', t') = -\mathrm{i}\langle \Psi^\uparrow(\mathbf{r}, t)\Psi^{*\downarrow}(\mathbf{r}', t')\rangle \tag{4.2}$$

where $\mathbf{r}, t$ $(\mathbf{r}', t')$ are the location and instant of the considered state, and Ψ is written in the Heisenberg formalism. In our case, after introducing a Fourier transform (to replace of the time variable t by the electron energy variable E), (4.2) gives:

$$\begin{aligned} G^{-+}_{\uparrow\downarrow}(\mathbf{r}, \mathbf{r}') = \int \mathrm{d}\epsilon \big\{ & f_L[\Psi_L^{\downarrow(\uparrow)*}(\mathbf{r}')\Psi_L^{\uparrow(\uparrow)}(\mathbf{r}) + \Psi_L^{\downarrow(\downarrow)*}(\mathbf{r}')\Psi_L^{\uparrow(\downarrow)}(\mathbf{r})] \\ & + f_R[\Psi_R^{\downarrow(\uparrow)*}(\mathbf{r}')\Psi_R^{\uparrow(\uparrow)}(\mathbf{r}) + \Psi_R^{\downarrow(\downarrow)*}(\mathbf{r}')\Psi_R^{\uparrow(\downarrow)}(\mathbf{r})]\big\} \end{aligned} \tag{4.3}$$

where $f_L = f^0(\epsilon)$ and $f_R = f^0(\epsilon + eV)$, and $f^0(\epsilon)$ is the Fermi distribution at 0 K, $\epsilon = E_\mathrm{F} - E$ and E is the tunnelling electron energy. In the Keldysh description, $\Psi_i^{\downarrow(\sigma)*}(\mathbf{r})\Psi_i^{\uparrow(\sigma)}(\mathbf{r})$ describes the contribution to the torque at the location $\mathbf{r}$ of an electron originally (i.e. at $t = -\infty$) in reservoir i with a spin state σ. Then, if an electron initially in the state σ gives a contribution to both the up-spin and the down-spin after propagation (the electron precesses around $\vec{S_\mathrm{d}}$ so that $\Psi_i^{\downarrow(\sigma)*}(\mathbf{r})$ and $\Psi_i^{\uparrow(\sigma)}(\mathbf{r})$ are non-zero), it induces a local effective magnetization and so exerts a torque on the background magnetization $\vec{S_\mathrm{d}}$. Otherwise, if it remains in a pure spin state (up or down), it does not induce any torque.

In an inhomogeneous structure, it is more convenient to use the mixed-coordinate system $(x - \vec{\kappa})$, where $\vec{\kappa}$ is the momentum parallel to the plane and x is the coordinate perpendicular to the plane. With $\mathbf{r} = (x, \vec{\rho})$, we get:

$$G^{-+}_{\uparrow\downarrow}(\mathbf{r}, \mathbf{r}') = \frac{a_0^2}{2\pi}\int_0^{2\sqrt{\pi}/a_0} \mathrm{e}^{\mathrm{i}\vec{\kappa}(\vec{\rho} - \vec{\rho'})} G^{-+}_{\uparrow\downarrow}(x, x')\,\mathrm{d}\vec{\kappa}. \tag{4.4}$$

The usual wavefunctions are determined quantum mechanically, using the WKB approximation following the usual procedure and solving the Schrödinger equation for Hartree–Fock spinor $\Psi = (\Psi^\uparrow, \Psi^\downarrow)$:

$$H\Psi = \left(\frac{p^2}{2m} - U - J_\mathrm{sd}(\vec{\sigma}\cdot\vec{S_\mathrm{d}})\right)\begin{pmatrix}\Psi^\uparrow \\ \Psi^\downarrow\end{pmatrix} = E\begin{pmatrix}\Psi^\uparrow \\ \Psi^\downarrow\end{pmatrix} \tag{4.5}$$

$\vec{S_\mathrm{d}}$ is the local magnetization of d-electrons in the ferromagnetic layer (F_L or F_R), $\vec{\sigma}$ is the vector in the Pauli matrix space: $\vec{\sigma} = \begin{pmatrix}\sigma^y \\ \sigma^z\end{pmatrix}$, E is the electron energy, U is the spin-independent potential across the entire junction, so that:

$(\vec{\sigma}\cdot\vec{S_\mathrm{d}}) = S_\mathrm{d}\sigma_z$ and $U = E_\mathrm{F}$ for $x < x_1$

$(\vec{\sigma}\cdot\vec{S_\mathrm{d}}) = 0$ and $U(x) = U_0 - \dfrac{x - x_1}{x_2 - x_1}eV$ for $x_1 < x < x_2$

$(\vec{\sigma}\cdot\vec{S_\mathrm{d}}) = S_\mathrm{d}(\sigma_z\cos\theta + \sigma_y\sin\theta)$ and $U = E_\mathrm{F} - eV$ for $x > x_2$.

Solving (4.5) allows us to obtain spin-dependent wavefunctions in each layer and, consequently, currents, IEC and STT as explained above. The spin-dependent wavefunctions are given in appendix B.

4.2.2. MTJ with impurities. A layer of impurities is now inserted within the insulating barrier of the MTJ. Each impurity is modelled as a local perturbation represented by a localized potential in the form $W(\mathbf{r}) = W\delta(\mathbf{r}-\mathbf{r}_0)$. $\mathbf{r}_0 = (x_0, \rho_0)$ is the spatial location of the impurities within the barrier and W the amplitude of their potential expressed in Å^{-1}. The equivalent energy of the impurity in eV is $E_i = \hbar^2 W/2ma_0$, where a_0 is the lattice parameter of the barrier. The impurities are randomly distributed in the plane $x = x_0$ parallel to the interfaces of the trilayer. In the spin-space representation, W is a 2×2 matrix, and in Keldysh formalism it is represented by a 4×4 matrix in the form $W\cdot\sigma^z$, where σ^z is the Pauli matrix.

We consider the case of low impurity concentration in the tunnel barrier, which means low coupling between impurities. This leads to a diagonal representation of the impurity matrix energy in spin-space:

$$W(\mathbf{r}) = W\delta(\mathbf{r}-\mathbf{r}_0) = \begin{pmatrix} W^{\uparrow} & 0 \\ 0 & W^{\downarrow} \end{pmatrix}.$$

Thus, in the Keldysh formalism:

$$W = \begin{pmatrix} W^{\uparrow} & 0 & 0 & 0 \\ 0 & W^{\downarrow} & 0 & 0 \\ 0 & 0 & -W^{\uparrow} & 0 \\ 0 & 0 & 0 & -W^{\downarrow} \end{pmatrix}.$$

In the case of a low concentration of impurities in the layer, it is sufficient to find the Green function for a single impurity considering the contribution of all impurities as additive. In this case, the Keldysh non-equilibrium perturbation technique gives rise to the expression for transverse effective local magnetic moment:

$$\begin{aligned} G^{-+}_{\uparrow\downarrow}(\mathbf{r},\mathbf{r}') = {} & G^{-+}_{0\uparrow\downarrow}(\mathbf{r},\mathbf{r}') - G^{-+}_{0\uparrow\uparrow}(\mathbf{r},\mathbf{r}_0)W^{\uparrow}G^{++}_{0\uparrow\downarrow}(\mathbf{r}_0,\mathbf{r}') - G^{-+}_{0\uparrow\downarrow}(\mathbf{r},\mathbf{r}_0)W^{\downarrow}G^{++}_{0\downarrow\downarrow}(\mathbf{r}_0,\mathbf{r}') \\ & + G^{--}_{0\uparrow\uparrow}(\mathbf{r},\mathbf{r}_0)W^{\uparrow}G^{-+}_{\uparrow\downarrow}(\mathbf{r}_0,\mathbf{r}') + G^{--}_{0\uparrow\downarrow}(\mathbf{r},\mathbf{r}_0)W^{\downarrow}G^{-+}_{\downarrow\downarrow}(\mathbf{r}_0,\mathbf{r}') \end{aligned} \tag{4.6}$$

where G^{α}_0 are the Keldysh, retarded and advanced Green functions evaluated without perturbation, given in appendix C. Using the usual relations $G^{++} = -G^A + G^{-+}$ and $G^{--} = G^R + G^{-+}$ [52], where G^A and G^R are the advanced and retarded Green functions, we obtain:

$$\begin{aligned} G^{-+}_{\uparrow\downarrow}(\mathbf{r},\mathbf{r}') = {} & G^{-+}_{0\uparrow\downarrow}(\mathbf{r},\mathbf{r}') + G^{-+}_{0\uparrow\uparrow}(\mathbf{r},\mathbf{r}_0)W^{\uparrow}G^{A}_{0\uparrow\downarrow}(\mathbf{r}_0,\mathbf{r}') + G^{-+}_{0\uparrow\downarrow}(\mathbf{r},\mathbf{r}_0)W^{\downarrow}G^{A}_{0\downarrow\downarrow}(\mathbf{r}_0,\mathbf{r}') \\ & + G^{R}_{0\uparrow\uparrow}(\mathbf{r},\mathbf{r}_0)W^{\uparrow}G^{-+}_{\uparrow\downarrow}(\mathbf{r}_0,\mathbf{r}') + G^{R}_{0\uparrow\downarrow}(\mathbf{r},\mathbf{r}_0)W^{\downarrow}G^{-+}_{\downarrow\downarrow}(\mathbf{r}_0,\mathbf{r}'). \end{aligned} \tag{4.7}$$

By the same procedure, we eliminate $G^{-+}_{\uparrow\downarrow}(\mathbf{r}_0,\mathbf{r}')$ and $G^{-+}_{\downarrow\downarrow}(\mathbf{r}_0,\mathbf{r}')$ from (4.7). This procedure gives an expression for $G^{-+}_{\uparrow\downarrow}(\mathbf{r},\mathbf{r}')$ as a function of non-perturbed Green functions $G_0(\mathbf{r},\mathbf{r}')$.

Finally, in the mixed-coordinate system, the transverse effective local magnetic moment is:

$$\begin{aligned} G^{-+}_{\uparrow\downarrow}(x,x) = {} & G^{-+}_{0\uparrow\downarrow}(x,x) + c\big[G^{-+}_{0\uparrow\uparrow}(x,x_0)W^{\uparrow}G^{A}_{\uparrow\downarrow}(x_0,x) + G^{-+}_{0\uparrow\downarrow}(x,x_0)W^{\downarrow}G^{A}_{\downarrow\downarrow}(x_0,x) \\ & + \frac{1}{\mathrm{Den}}\big\{\big[W^{\uparrow}G^{R}_{0\uparrow\uparrow}(x,x_0)(1 - W^{\downarrow}G^{R}_{0\downarrow\downarrow}(\mathbf{r}_0,\mathbf{r}_0)) \\ & + W^{\uparrow}W^{\downarrow}G^{R}_{0\uparrow\downarrow}(x,x_0)G^{R}_{0\downarrow\uparrow}(\mathbf{r}_0,\mathbf{r}_0)\big] \\ & \times \big[G^{-+}_{0\uparrow\downarrow}(x_0,x) + W^{\uparrow}G^{-+}_{0\uparrow\uparrow}(\mathbf{r}_0,\mathbf{r}_0)G^{A}_{\uparrow\downarrow}(x_0,x') + W^{\downarrow}G^{-+}_{0\uparrow\downarrow}(\mathbf{r}_0,\mathbf{r}_0)G^{A}_{\downarrow\downarrow}(x_0,x)\big] \\ & + \big[W^{\downarrow}G^{R}_{0\uparrow\downarrow}(x,x_0)(1 - W^{\uparrow}G^{R}_{0\uparrow\uparrow}(\mathbf{r}_0,\mathbf{r}_0)) + W^{\uparrow}W^{\downarrow}G^{R}_{0\uparrow\uparrow}(x,x_0)G^{R}_{0\uparrow\downarrow}(\mathbf{r}_0,\mathbf{r}_0)\big] \\ & \times \big[G^{-+}_{0\downarrow\downarrow}(x_0,x) + W^{\uparrow}G^{-+}_{0\downarrow\uparrow}(\mathbf{r}_0,\mathbf{r}_0)G^{A}_{\uparrow\downarrow}(x_0,x) + W^{\downarrow}G^{-+}_{0\downarrow\downarrow}(\mathbf{r}_0,\mathbf{r}_0)G^{A}_{\downarrow\downarrow}(x_0,x)\big]\big\}\big] \end{aligned} \tag{4.8}$$

where c is the impurity concentration and

$$\mathrm{Den} = \left[1 - W^{\uparrow} G^{R}_{0\uparrow\uparrow}(\mathbf{r}_0, \mathbf{r}_0)\right] \times \left[1 - W^{\downarrow} G^{R}_{0\downarrow\downarrow}(\mathbf{r}_0, \mathbf{r}_0)\right] - W^{\uparrow} W^{\downarrow} G^{R}_{0\uparrow\downarrow}(\mathbf{r}_0, \mathbf{r}_0) G^{R}_{0\downarrow\uparrow}(\mathbf{r}_0, \mathbf{r}_0)$$

$$G^{\alpha}_{\sigma\sigma'}(\mathbf{r}_0, \mathbf{r}_0) = \frac{a_0^2}{2\pi} \int_0^{2\sqrt{\pi}/a_0} G^{\alpha}_{\sigma\sigma'}(x_0, x_0)\kappa \, \mathrm{d}\kappa.$$

This denominator appears when replacing $G^{-+}_{\uparrow\downarrow}(\mathbf{r}_0, \mathbf{r}')$ and $G^{-+}_{\downarrow\downarrow}(\mathbf{r}_0, \mathbf{r}')$ by their expressions as a function of the non-perturbed Green functions. The determination of the non-perturbed Green function is performed solving the Dyson equation of the MTJ:

$$(E - H)G(\mathbf{r}, \mathbf{r}') = \delta(\mathbf{r} - \mathbf{r}') \tag{4.9}$$

where H is the Hamiltonian of the structure (see (4.5)) and $G(\mathbf{r}, \mathbf{r}')$ is the 2×2 Green function matrix in spin space. The non-perturbed and perturbed Green functions are given in appendices C and D, respectively.

4.2.3. Currents and torques. Spin transfer torque and interlayer exchange coupling can now be determined from (4.8), whereas spin-dependent electrical currents are calculated from the usual local definition:

$$m_x + \mathrm{i}m_y = \frac{J_{\mathrm{sd}}}{\mu_{\mathrm{B}}} \langle \sigma^{+} \rangle = \frac{J_{\mathrm{sd}}}{\mu_{\mathrm{B}}} \frac{a_0^3}{(2\pi)^2} \int \int G^{-+}_{\uparrow\downarrow}(x, x, \epsilon)\kappa \, \mathrm{d}\kappa \, \mathrm{d}\epsilon \tag{4.10}$$

$$m_z = \frac{J_{\mathrm{sd}}}{\mu_{\mathrm{B}}} \frac{a_0^3}{(2\pi)^2} \int \int \left[G^{-+}_{\uparrow\uparrow}(x, x, \epsilon) - G^{-+}_{\downarrow\downarrow}(x, x, \epsilon)\right] \kappa \, \mathrm{d}\kappa \, \mathrm{d}\epsilon \tag{4.11}$$

$$J_{\uparrow(\downarrow)} = \frac{\hbar e}{4\pi m} \int \int \left[\frac{\partial}{\partial x} - \frac{\partial}{\partial x'}\right] G^{-+}_{\uparrow\downarrow}(x, x', \epsilon)|_{x=x'} \kappa \, \mathrm{d}\kappa \, \mathrm{d}\epsilon \tag{4.12}$$

$$J = J_{\uparrow} + J_{\downarrow} \tag{4.13}$$

where $J_{\uparrow(\downarrow)}$ is the spin-up(-down) electrical current. $G^{-+}_{\uparrow\uparrow}(x, x, \epsilon)$ and $G^{-+}_{\downarrow\downarrow}(x, x, \epsilon)$ are the energy-resolved local density-of-states (LDOS) for up- and down-spins respectively, whereas $\int G^{-+}_{\uparrow\uparrow}(x, x, \epsilon) \, \mathrm{d}\epsilon$ and $\int G^{-+}_{\downarrow\downarrow}(x, x, \epsilon) \, \mathrm{d}\epsilon$ give the number of up- and down-electrons at the location x along the structure.

It is clear that due to the s–d exchange interaction, to the non-collinearity of the d-electron magnetization $\vec{S_{\mathrm{d}}}$ and to the non-equilibrium magnetization of the s-electrons, an additional torque $\vec{T}$ appears which acts on the magnetization of the layer. This torque may be written as

$$\vec{T} = -\gamma \left[\vec{S_{\mathrm{d}}} \times \vec{m}\right] \tag{4.14}$$

where the non-equilibrium magnetization $\vec{m}$ is evaluated from (4.10) and (4.11). In the following, we will assume that $\vec{S_{\mathrm{d}}}$ has only z and x components not equal to zero. The non-equilibrium magnetization $\vec{m}$ has all its three components different from zero. The m_x term yields an additional exchange between the magnetizations of the free and pinned layers, as already discussed by Slonczewski [10], and m_y is responsible for the new type of torque which acts as a damping or antidamping term in the LLG equation (2.7).

4.3. Results: no impurities in the barrier

In the following, the material parameters taken for the simulations are as follows: $k_{\mathrm{F}}^{\uparrow} = 1.1$ Å^{-1}, $k_{\mathrm{F}}^{\downarrow} = 0.6$ Å^{-1} are the spin-up and spin-down Fermi wavevectors, respectively, in the ferromagnets; the height of the barrier is $U - E_{\mathrm{F}} = 2.44$ eV ($q_0 = 0.8$ Å^{-1} is the insulator wavevector) and its thickness is $d = x_2 - x_1 = 7$ Å. The bias voltage applied to the junction is denoted as V_{b}. The effective electron mass is set to 1 for simplicity. However,

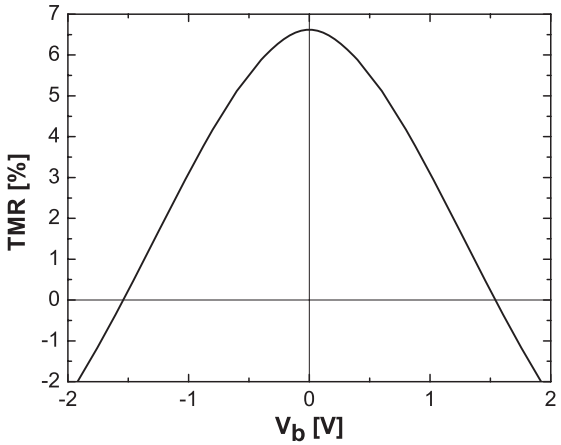

Figure 7. Tunnel magnetoresistance versus bias voltage V_b. The parameters of the ferromagnetic electrodes are $k_F^{\uparrow} = 1.1$ Å^{-1}, $k_F^{\downarrow} = 0.6$ Å^{-1}, the barrier height is $U = 2.44$ eV and its thickness is $d = 7$ Å.

to fit experimental results, we will have to consider that the electron mass in the insulator is smaller than the electron mass in the electrodes [54]. In the following, we evaluate STT and IEC in the left ferromagnet for a positive voltage. To evaluate these quantities at negative bias voltage, it is equivalent to calculate them in the right electrode for positive bias, since the MTJ is symmetric.

Positive bias means that electrons flow from the left to the right electrode, whereas at negative bias, electrons flow from the right to the left electrode.

4.3.1. Currents and TMR. Figure 7 shows the bias dependence of tunnel magnetoresistance. The TMR shows the usual decay and an inversion at high bias voltage. This decrease is attributed to the bias dependence of the interfacial polarization factors [55]. The inversion of TMR has been observed experimentally [56] and is attributed to a bias dependence of the coupling between ferromagnetic states.

The tunnel conductivity increases much more quickly with bias voltage in an antiparallel configuration (AP) than in a parallel configuration (P). The bias voltage at which the conductivity in AP exceeds the conductivity in P can be estimated from the coherent tunnelling coefficient [55]:

$$D(\epsilon, \kappa, V) = q(\epsilon, \kappa, V)^2 - k_{\uparrow}(\epsilon, \kappa, V)k_{\downarrow}(\epsilon, \kappa, V)$$

where q is the barrier wavevector and $k_{\uparrow(\downarrow)}$ is the up (down)-spin wavevector at the interface.

Figure 8 shows the bias dependence of spin-up (black) and spin-down (grey) currents for positive voltage. It can be seen that at low bias, down-spin current in the AP configuration exceeds down-spin current in the P configuration, and around $V_b = 0.48$ V it reverses. However, the up-spin current in the P configuration first exceeds up-spin current in the AP configuration and then, around $V_b = 0.95$ V, the up-spin current in AP exceeds the up-spin current in P. Furthermore, the up-spin current is always higher than the down-current. Globally, for a particular bias voltage, electrical current becomes higher at high bias voltage in the AP configuration than in the P configuration.

4.3.2. Torques in MTJ. The angular dependence of IEC and STT is investigated first. At fixed bias and fixed location in the left ferromagnetic layer, we calculated IEC and STT as a

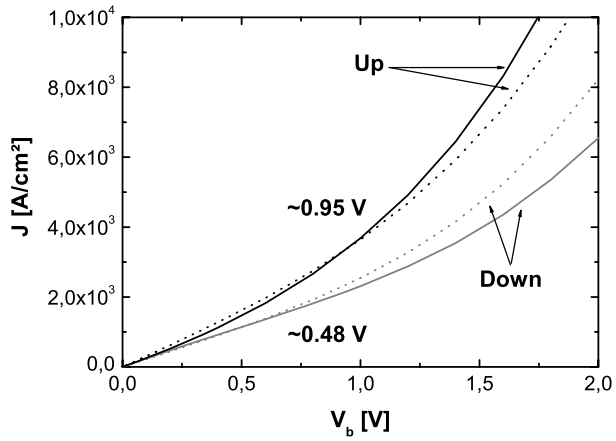

Figure 8. Spin-up (black line) and spin-down (grey line) currents versus bias voltage V_b in parallel (dotted line) and antiparallel (solid line) configuration. The parameters are the same as in figure 7.

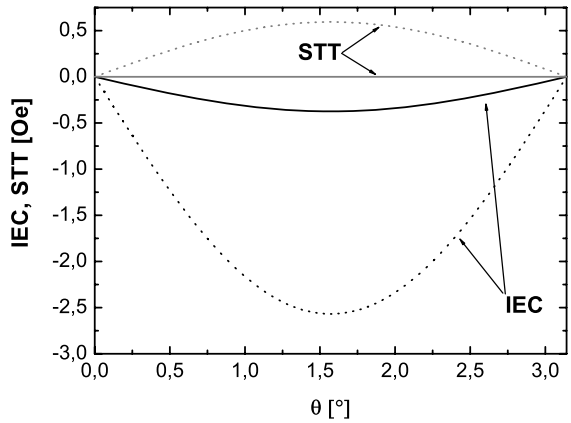

Figure 9. Angular dependence of IEC (black lines) and STT (grey lines) at $z = -6$ Å, with $V_b = 0$ V (solid lines) and $V_b = 1$ V (dotted lines). The parameters are the same as in figure 7.

function of the angle θ between the magnetizations of the left and right ferromagnets. The plot is reported in figure 9. This figure shows that STT vanishes at zero bias, contrary to IEC, and both IEC and STT present an angular dependence in the form STT, IEC $= \alpha \sin(\theta)$. The deviation from this form is lower than 10^{-4}, so a sine curve is a good approximation. In the following we estimate spin torque and coupling at $\theta = 90°$.

We then calculated the x dependence of spin transfer torque and exchange coupling in the left ferromagnetic layer for a fixed bias voltage ($V_b = 1$ V). Spin torque is represented by a black line in figure 10. The oscillating and damping behaviour illustrates the interferences between tunnelling and reflected electrons, with an oscillation period of $T = 2\pi/(k_F^{\uparrow} - k_F^{\downarrow})$. The dotted line shows the averaged spin torque as a function of the thickness of the left ferromagnet $\mathrm{STT}_{\mathrm{ave}} = \int_{x_1}^{x} \mathrm{STT}(x')\,\mathrm{d}x'/(x_1 - x)$. We find an important averaged STT in the first nanometre from the interface, then spin torque decreases and reaches zero around $x_1 - x = 20$ nm. We have to remember that the ballistic assumption holds within a distance from the interface equal to the mean free path λ of the ferromagnet (typically $\lambda \approx 5$ nm in Co). Anyway, the averaged spin torque is nearly zero at a thickness of 5 nm, so diffusion has no impact here.

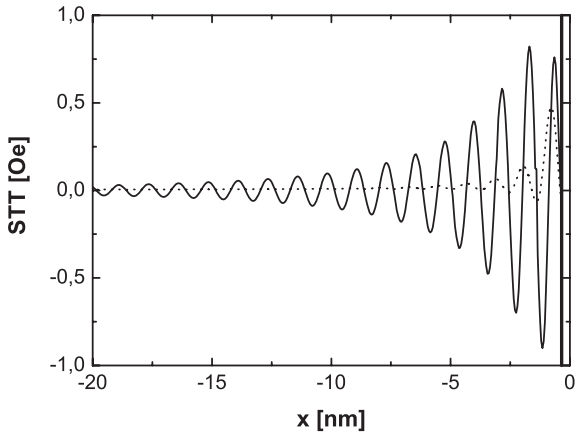

Figure 10. Spin transfer torque (solid line) versus location in the left ferromagnet calculated at $V_b = 1$ V and corresponding averaged spin transfer torque (dotted line) versus thickness of the left ferromagnet. The parameters are the same as in figure 7.

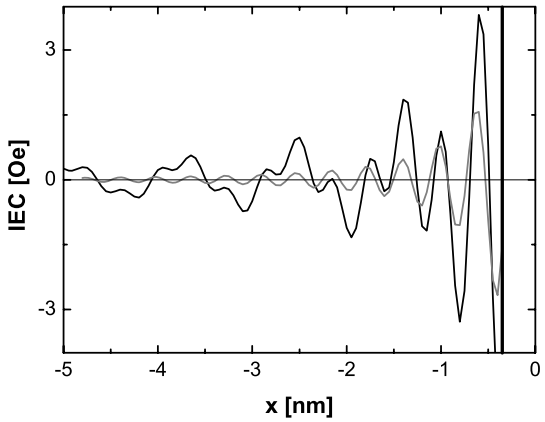

Figure 11. Interlayer exchange coupling versus location in the left ferromagnet calculated at $V_b = 0$ V (grey line) and $V_b = 1$ V (black line). The parameters are the same as in figure 7.

Similarly, in figure 11 we evaluated IEC in the left ferromagnet at $V_b = 0$ V (grey curve) and $V_b = 1$ V (black curve). The oscillations of IEC versus location exhibit a single period at zero bias. However, when applying a bias voltage, $V_b = 1$ V, a beating appears with periods of the oscillations equal to $T_1 = 2\pi/(k_F^{\uparrow} - k_F^{\downarrow})$ and $T_2 = 2\pi/(k_F^{\uparrow} + k_F^{\downarrow})$ which correspond to the two interference frequencies, as expected.

Figure 12 shows the x dependence of IEC, and its averaged value $\mathrm{IEC}_{\mathrm{ave}} = \int_{x_1}^{x} \mathrm{IEC}(x')\,\mathrm{d}x'/(x_1 - x)$. We find that the averaged exchange coupling oscillates as a function of x but decays within the first nanometre in the layer, as for STT. Nevertheless, averaged IEC remains higher than averaged STT, as shown in figure 13.

We also plotted the bias voltage dependence of the spin transfer torque and interlayer exchange coupling in figure 14. An important asymmetry appears for STT, consistently with Slonczewski's work [21].

Furthermore, STT reverses around $V_b = 1.33$ V and IEC, which remains negative as a function of bias, is about two to four times higher than STT. We can compare this behaviour

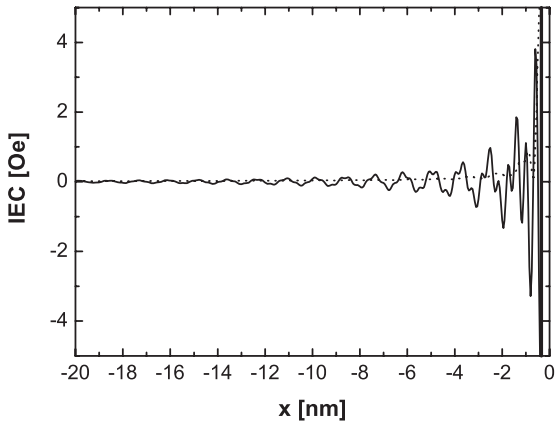

Figure 12. Interlayer exchange coupling versus location in the left ferromagnet calculated at $V_b = 1$ V (solid line) and corresponding averaged interlayer exchange coupling (dotted line) versus thickness of the left ferromagnet. The parameters are the same as in figure 7.

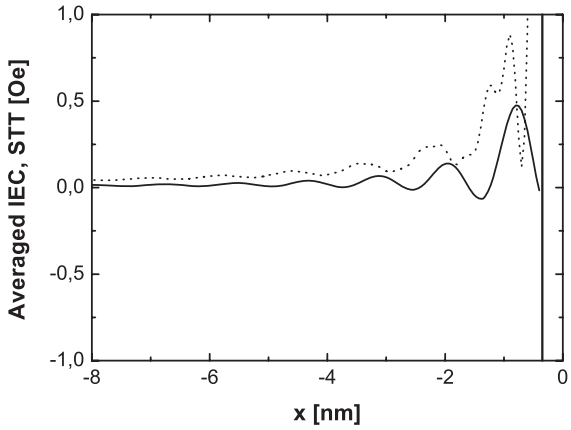

Figure 13. Comparison between averaged IEC (dotted line) and averaged STT (black line) as a function of the layer thickness. The parameters are the same as in figure 7.

with the situation shown in figure 15, where the height of the barrier is lower and set to $U - E_F = 1$ eV. This time, STT still shows an important asymmetry, but does not reverse (even at higher voltage) and IEC shows a linear bias dependence for low voltage and reverses for negative bias. This time, both STT and IEC increase compared to the case of a high barrier and IEC can be two orders of magnitudes higher than STT. Effective mass also plays an important role in the bias dependence and the ratio between STT and IEC.

We now focus on the asymmetry of STT as a function of bias, with is of great interest for experimentalists. Figures 16 and 17 shows the absolute value of STT versus bias voltage for $U - E_F = 2.44$ eV and 1 eV, respectively. We find that STT is always higher at negative bias, where the main contribution to spin torque comes from direct tunnelling electrons.

This asymmetry has been attributed by Slonczewski [21] to the bias dependence of the spin-dependent interfacial density of states (DOS). Indeed, in a very simple approach, STT in the left layer is proportional to the spin polarization in the right layer, and so to the DOS of the right electrode. Moreover, the interfacial spin-dependent DOS in the right electrode

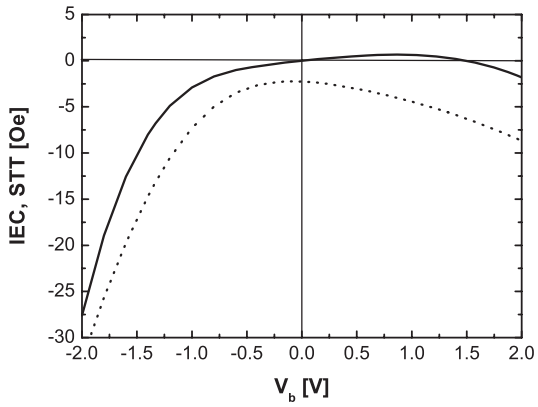

Figure 14. Spin transfer torque (solid line) and interlayer exchange coupling (dotted line), averaged on 1 nm, versus bias voltage V_b. The barrier height is set to $U - E_F = 2.44$ eV.

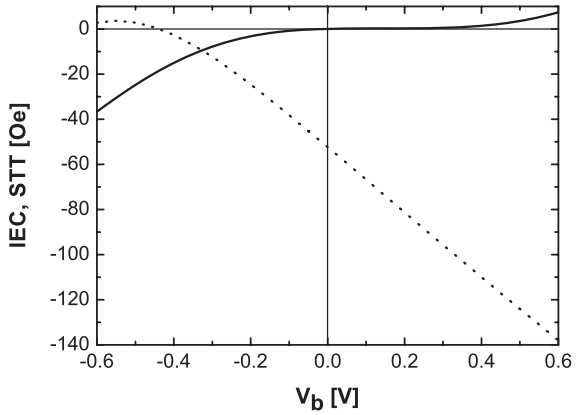

Figure 15. Spin transfer torque (solid line) and interlayer exchange coupling (dotted line), averaged on 1 nm from the interface, versus bias voltage V_b. The barrier height is set to $U - E_F = 1$ eV.

strongly depends on positive bias voltage but only weakly on negative bias voltage. Then, STT should be asymmetric in voltage. This idea is illustrated by the calculations shown in figure 18. The bias dependence of left (solid line) and right (dotted line) interfacial polarizations $P = \left[D^{\uparrow}(E_F) - D^{\downarrow}(E_F)\right] / \left[D^{\uparrow}(E_F) + D^{\downarrow}(E_F)\right]$, where $D^{\uparrow(\downarrow)}(E_F)$ is the up- (down-) spin interfacial DOS at Fermi energy. The left interfacial DOS (and thus spin polarization) depends only weakly on positive bias, whereas the right interfacial DOS depends strongly on it.

4.3.3. Linear relationship. Figure 19 (figure 20) shows the variation of spin torque versus absolute TMR (defined as $\Delta J = J_P - J_{AP}$) when varying the barrier thickness d (height q_0). A clearly linear relationship is found in both figures. It can also be seen that this linear slope extrapolates to zero when absolute TMR goes to zero [57]. The top (bottom) insets of figures 20 and 19 show the variation of absolute TMR (spin torque) versus barrier height and barrier thickness, respectively. However, as shown in the left part of the slope in figure 19, this relation is no longer true at smaller values of spin torque (namely, for thick barriers).

Similarly to section 3, this linear dependence means that spin torque and magnetoresistance have the same physical origin, i.e. spin polarization.

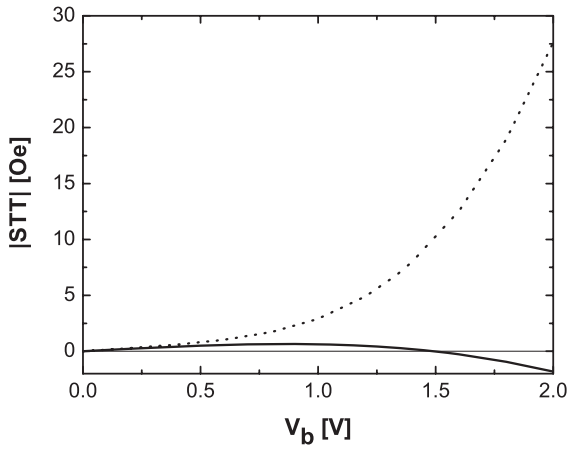

Figure 16. Magnitude of spin transfer torque as a function of absolute bias calculated in the left ferromagnet and averaged on 1 nm from the interface, for positive (solid line) and negative (dotted line) bias voltage. The barrier height is set to $U - E_F = 2.44$ eV.

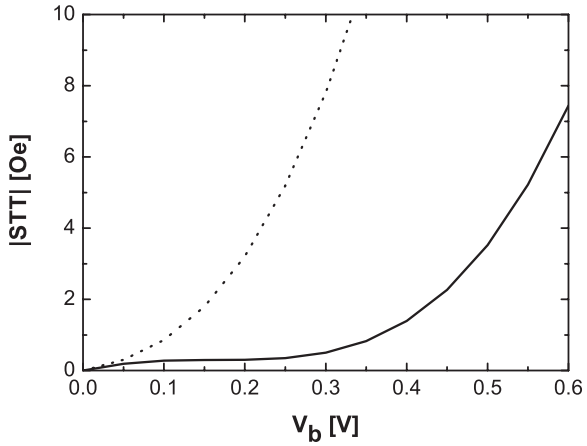

Figure 17. Magnitude of spin transfer torque as a function of absolute bias calculated in the left ferromagnet and averaged on 1 nm from the interface, for positive (solid line) and negative (dotted line) bias voltage. The barrier height is set to $U - E_F = 1$ eV.

4.4. Results: barrier with impurities

4.4.1. Impurity-induced resonance. The introduction of a layer of impurities in the barrier creates a quantum well with an energy depth (evaluated from the top of the insulating barrier) of $E_i = \hbar^2 W/2ma_0$. The location of the impurity in the barrier is given by $x_0 \in [x_1, x_2]$. The concentration of the impurities randomly distributed in the plane parallel to the plane of the structure is $c = 3\%$, so that we can neglect the coupling between impurities.

In (4.8), the denominator Den is a function of the electron energy E and of the amplitude of the impurity potential W, so it can reach the minimum (almost zero value) for a given electron energy E (for example E_F) at some value of W. Figure 21 shows the impurity energy dependence of the inverse absolute value of the denominator at $E = E_F$. It shows a sharp resonance peak for a particular value of impurity energy. Figure 22 shows the intensity

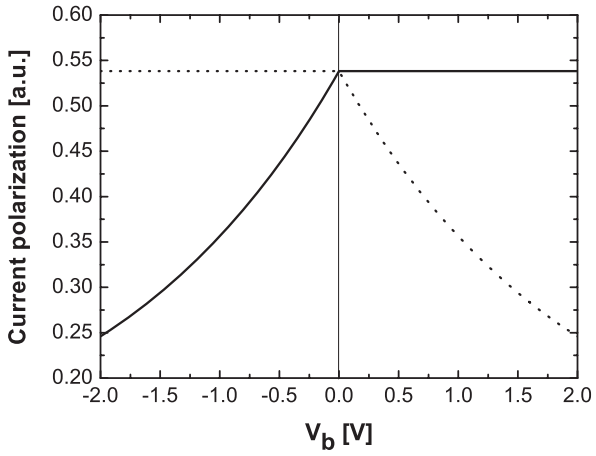

Figure 18. Left (solid line) and right (dotted line) interfacial current polarization versus bias voltage. The barrier height is set to $U - E_F = 1$ eV.

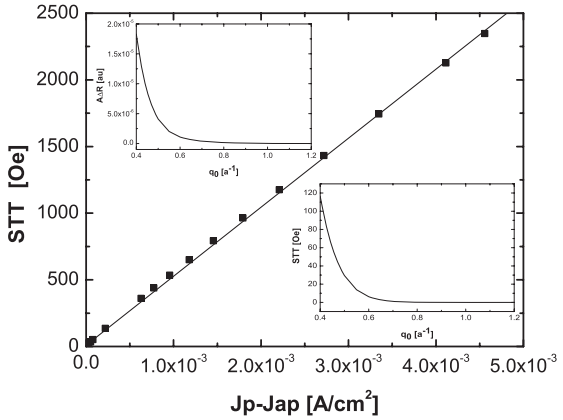

Figure 19. Spin torque versus absolute TMR when varying the barrier thickness. The top (bottom) inset shows the absolute TMR (spin torque) versus the barrier thickness. The barrier height is set to $U - E_F = 2.44$ eV.

of $1/|\text{Den}|$ together with the resonance impurity energy as a function of the location of the impurity layer in the barrier. These values were calculated for a bias voltage of $V_b = 1$ V, a barrier height of $U - E_F = 2.44$ eV and a barrier thickness of $d = 7$ Å. It can be seen that the maximum of resonance is reached when the impurity layer is inserted close to the middle of the barrier. The small shift from the middle of the barrier is due to the applied bias voltage which breaks the MTJ symmetry.

This resonance induces a peak in the spin transfer torque and current-driven interlayer exchange coupling which is reported in figure 23. This simulation was done at $V_b = 1$ V and $x_0 = -2$ Å. A sharp peak in STT appears around $E_R = -5.133$ eV. It is interesting to note that at this point the IEC changes its sign. One must remember that STT $\propto$ Im($\langle\sigma_+\rangle$) and IEC $\propto$ Re($\langle\sigma_+\rangle$) and it is possible to express $\langle\sigma_+\rangle$ near the resonance as

$$\langle\sigma_+\rangle = \frac{1}{(W - W_R) + \mathrm{i}\alpha}. \tag{4.15}$$

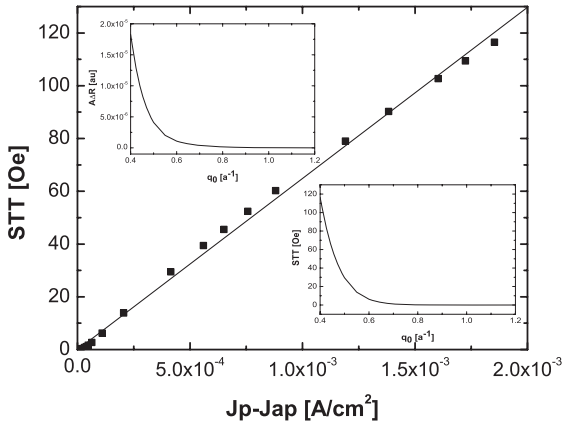

Figure 20. Spin torque versus absolute TMR when varying the barrier height. The top (bottom) inset shows the absolute TMR (spin torque) versus the barrier height. The barrier thickness is set to $x_2 - x_1 = 7$ Å.

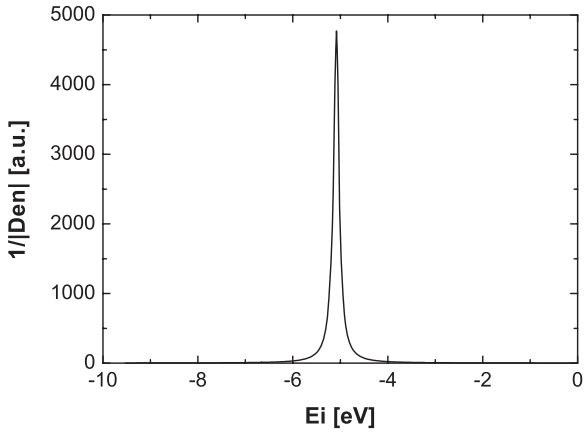

Figure 21. Absolute inverse denominator $1/|\mathrm{Den}|$ as a function of the impurity energy. We use $x_0 = -2$ Å, $V_\mathrm{b} = 1$ V, $U - E_\mathrm{F} = 2.44$ eV and $d = 7$ Å. We set $\kappa = 0$ and $\epsilon = 0$.

This expression can be obtained from 4.8 neglecting the $G_{\uparrow\downarrow}$ terms near the resonance. It is immediately clear that STT and IEC stand, respectively, for the dissipative and conservative part of $\langle\sigma_+\rangle$ and this explains the above mentioned behaviour. A more accurate study of resonance of STT and IEC will be addressed below.

To evaluate the influence of this resonance on spin torque and exchange coupling, we investigate the dependence of STT and IEC on the location in the left layer. Figure 24 shows the influence of impurity-induced resonance on the oscillating behaviour of STT in the left layer. A convenient way to measure the influence of the impurity resonance is to investigate its influence on the averaged spin torque (see figure 25). It can be seen that spin torque is enhanced by a factor of 40 within the first nanometre, when the impurity is located at $x_0 = -1.5$ Å. Moreover, the closer to the middle of the barrier ($x_0 = 0$ Å) the impurity is, the higher the spin torque (see figure 22).

The dependence of spin torque on the bias voltage for different locations of the impurity layer, in figure 26, shows an important enhancement. For example, without impurities, at

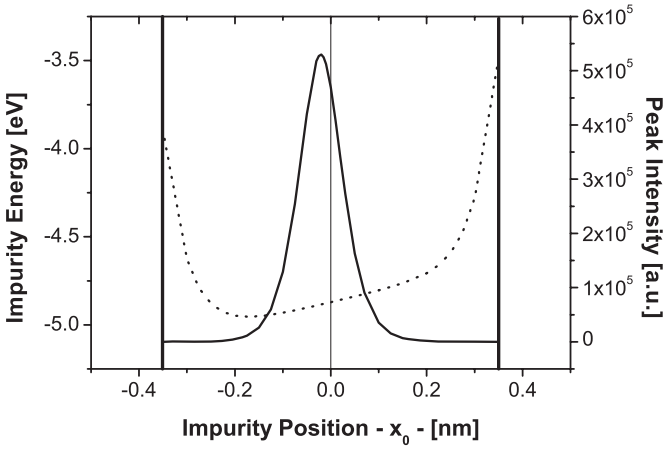

Figure 22. Intensity (solid line) and impurity resonance energy (dotted line) versus location of the impurity inside the barrier, calculated at $V_b = 1$ V, $U - E_F = 2.44$ eV and $d = 7$ Å.

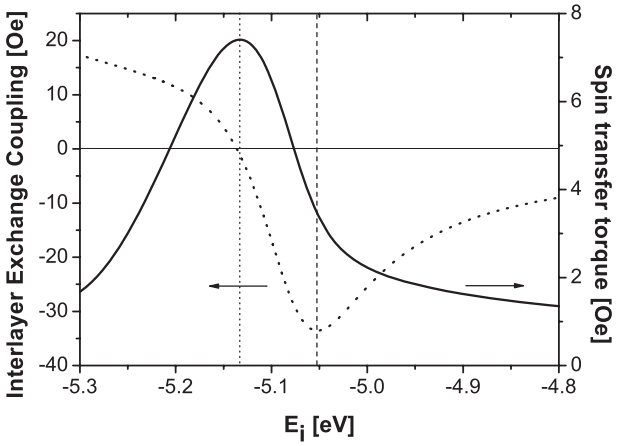

Figure 23. Current-driven interlayer exchange coupling (dotted line) and spin transfer torque (solid line) versus impurity energy. We use $x_0 = -2$ Å, $V_b = 1$ V, $U - E_F = 2.44$ eV and $d = 7$ Å.

$V_b = 2$ V, $J_e = 1.97 \times 10^4$ A cm^{-2} and STT $= 2.36$ Oe, whereas with an impurity located at $x_0 = -2$ Å (green curve in figure 26), $J_e = 5.5 \times 10^5$ A cm^{-2} and STT $= 169$ Oe. This comparison shows that the role of impurity resonance is not only to increase the current flowing across the junction: it has a more fundamental impact on spin-polarized current.

This is illustrated by figure 27, where the absolute tunnel magnetoresistance ($\Delta J = J_P - J_{AP}$) is plotted as a function of the impurity energy. It shows a peak corresponding to the maximum of spin torque. However, the energy resonance for TMR ($\approx$5.1 eV) is not exactly the energy resonance of STT ($\approx$5.133 eV). Tsymbal *et al* [48] proposed interesting studies of impurity-induced TMR resonance in a MTJ. We notice that compared to TMR without impurities, the TMR calculated at STT resonance ($E_i = -5.133$ eV) is lower below $V_b = 1.2$ V, then exceeds TMR without impurities above 1.2 V (see figure 28).

A preliminary understanding of the origin of STT resonance is given by the impurity energy dependence of the spin-dependent electrical current at $\theta = 90°$, shown in figure 29. This figure shows an important enhancement of the total current around E_R, but also shows

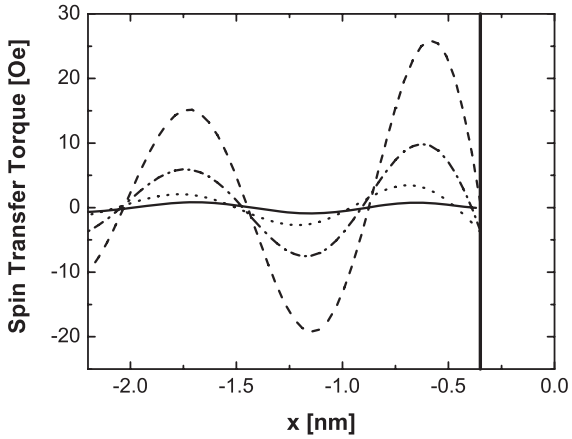

Figure 24. Spin transfer torque versus location in the left ferromagnet: (solid line) without impurities, (dotted line) $x_0 = -2.5$ Å at resonance, (dashed–dotted line) $x_0 = -2$ Å at resonance, (dashed line) $x_0 = -1.5$ Å at resonance. The calculation have been perform at $V_b = 1$ V.

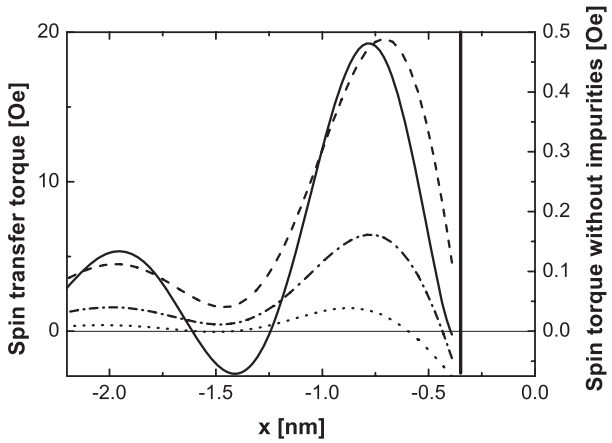

Figure 25. Average spin transfer torque versus location in the left ferromagnet: (solid line) without impurities, (dotted line) $x_0 = -2.5$ Å at resonance, (dashed–dotted line) $x_0 = -2$ Å at resonance, (dashed line) $x_0 = -1.5$ Å at resonance. The calculations have been performed at $V_b = 1$ V.

that spin-down electrical current exceeds spin-up electrical current and reaches a maximum at the resonance energy E_R. This means that in the magnetic configuration for which we calculate STT, the transverse spin asymmetry is maximum at impurity resonance.

4.4.2. Spin-dependent density of states. To further understand this resonance phenomenon, we investigated the number of spins located at the impurity site $\mathbf{r}_0$ as a function of the impurity energy. Figure 30 presents the absolute number of spins $n_{\uparrow(\downarrow)}$ as a function of impurity energy. Actually, $n_{\uparrow(\downarrow)}$ is the difference between the number of spins at zero bias and the number of spins at $V_b = 1$ V:

$$n_{\uparrow(\downarrow)} = n_{\uparrow(\downarrow)}(V_b = 1\text{ V}) - n_{\uparrow(\downarrow)}(V_b = 0\text{ V}).$$

We find a feature similar to the spin-dependent current in figure 29. The number of down electrons located on the impurity exceeds the number of up electrons at the impurity resonance.

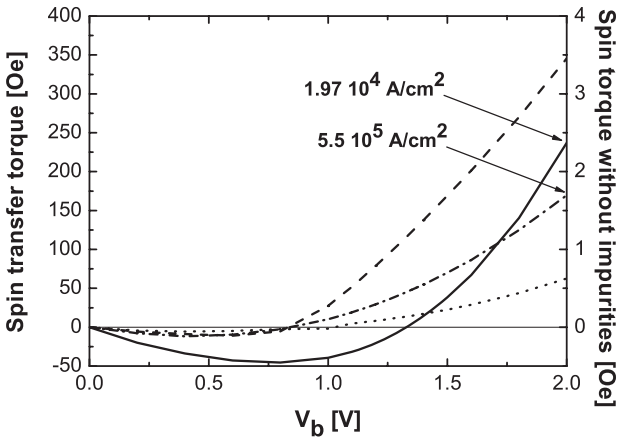

Figure 26. Spin transfer torque versus bias voltage V_b: (solid line) without impurities, (dotted line) $x_0 = -2.5$ Å at resonance, (dashed–dotted line) $x_0 = -2$ Å at resonance, (dashed line) $x_0 = -1.5$ Å at resonance. The calculations have been performed at $V_b = 1$ V.

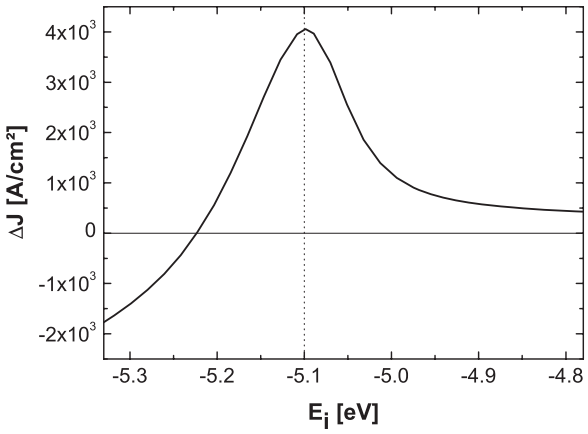

Figure 27. Absolute tunnel magnetoresistance versus impurity energy at $V_b = 1$ V and $x_0 = -2$ Å.

The shape of $n_{\uparrow(\downarrow)}$ gives important information concerning the coupling process. $n_\uparrow$ presents a wider and lower Lorentzian-like curve than $n_\downarrow$. The width of the curve is due to the coupling between spin-dependent states in the ferromagnets and metallic states of the impurity. Consequently, the number of up-electrons located at the impurity site is distributed over a wider energy range than down-electrons. Then, because the distribution of down-electrons over the impurity energy range is narrower than up-electrons, at resonance there is a maximum of down-electrons on the impurity site, and it exceeds the number of up-electrons. As a consequence, the spin imbalance is increased and transverse spin current is maximum at resonance. An equivalent interpretation is that the spin of an electron impinging on the impurity site precesses around an effective exchange field [58]. The effective field located on the impurity originates from the interaction between the external electrodes and the impurity.

We carry on our investigation focusing on the spin-dependent local density of state (LDOS) of the spins at the location of the impurity. Figure 31 shows the energy-resolved LDOS for up and down spins at $x_0 = -2$ Å, $V_b = 1$ V and $E_R = -5.133$ eV. It is shown that the peak of

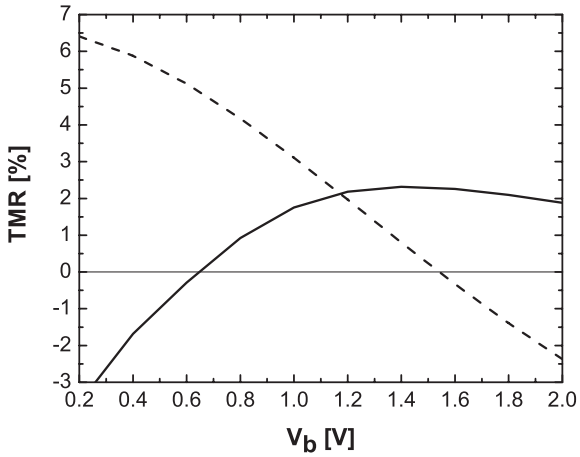

Figure 28. Comparison between the bias dependence of absolute TMR without impurities (dashed line) and at STT resonance (solid line). The resonance is calculated at $x_0 = -2$ Å and $V_b = 1$ V.

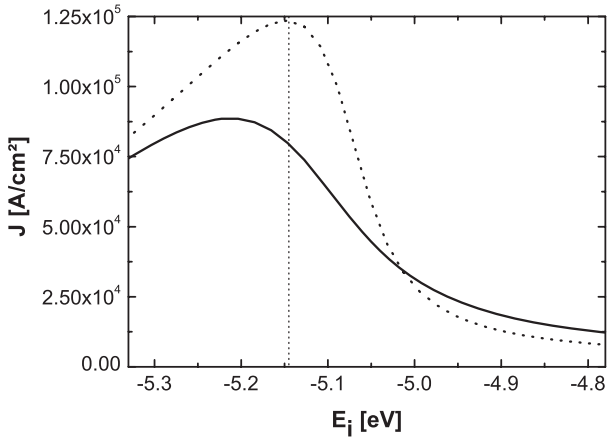

Figure 29. Spin-up (solid line) and spin-down (dotted line) current at $\theta = 90°$ versus impurity energy at $x_0 = -2$ Å and $V_b = 1$ V.

up-electrons is centred on the Fermi energy, whereas the peak of down-electrons is below the Fermi energy. This means that the main contribution comes from electrons originating near the Fermi energy and that the spin asymmetry comes from the down-electrons located just below the Fermi energy.

We also notice that at the Fermi energy, spin-up and spin-down LDOS are equal. This is confirmed by the impurity energy dependence of spin-dependent LDOS at Fermi energy shown in figure 32.

As a comparison, the dotted vertical line in figure 32 represents the impurity energy resonance for STT and the dashed vertical line the resonance of IEC (see correspondence in figure 23). Calculating the spin asymmetry $P = \left[D^{\uparrow}(E_F) - D^{\downarrow}(E_F)\right] / \left[D^{\uparrow}(E_F) + D^{\downarrow}(E_F)\right]$ on the impurity site, at the Fermi energy, as a function of the impurity energy, we find an interesting behaviour, reported in figure 33. We find that at STT resonance (dotted vertical line), the Fermi electrons present a zero spin asymmetry, whereas at IEC resonance (dashed

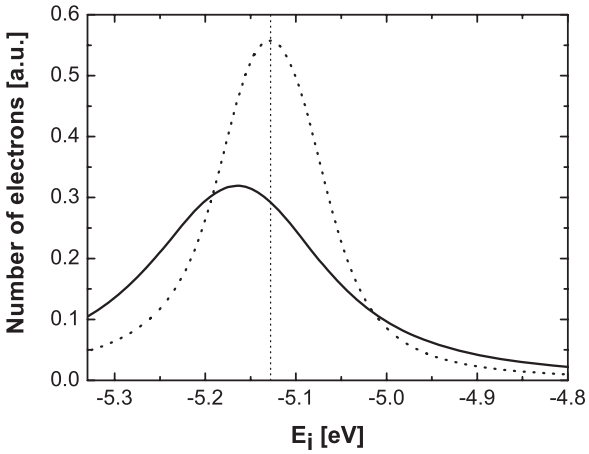

Figure 30. Number of up (solid line) and down (dotted line) electrons at the impurity location versus impurity energy at $x_0 = -2$ Å and $V_b = 1$ V.

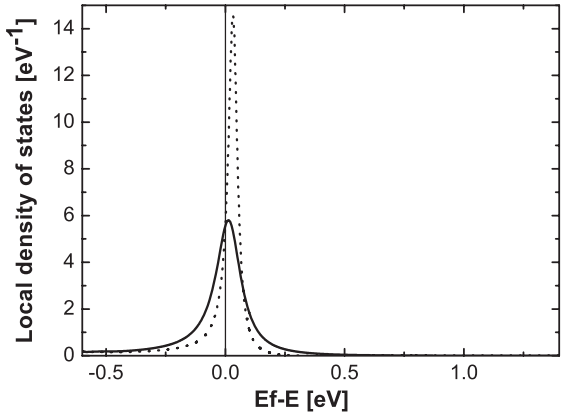

Figure 31. Spin-dependent local density of states at the STT resonance versus electron energy at $x_0 = -2$ Å, $E_R = -5.133$ eV and $V_b = 1$ V for spin-up (solid line) and spin-down (dotted line).

vertical line) this asymmetry reaches a maximum. Furthermore, as we noted previously, at STT resonance IEC changes its sign, which corresponds to a change of sign of the spin asymmetry.

We can conclude that the resonance feature of STT can be explained considering the contribution of the electrons located near the Fermi level, which is consistent with the previous works [21]. IEC resonance is driven by the electrons close to the Fermi energy. This can be understood considering the energy-resolved LDOS at IEC resonance in figure 34. We see that the resonant peak of down electrons is centred on the Fermi level, whereas the peak of up electrons is above the Fermi level. Thus, whereas IEC is usually attributed to the contribution of all the electrons below the Fermi level, the resonance seems to be driven by electrons at the Fermi energy.

These interesting features emphasize the possibility of dramatically increasing the spin torque and interlayer exchange coupling by controlling the impurity doping of the insulating barrier, and that it is possible to reduce IEC while increasing STT. However, because TMR

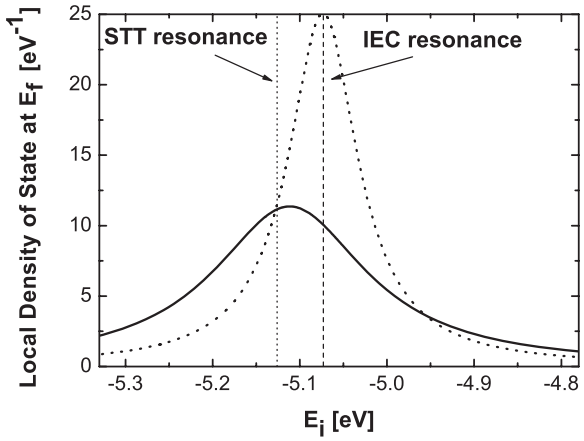

Figure 32. Spin-dependent local density of state at the Fermi energy for up (solid line) and down (dotted line) electrons versus impurity energy at $x_0 = -2$ Å and $V_b = 1$ V. The vertical dotted line and dashed line represent the energy of impurity-induced resonance for STT and IEC, respectively.

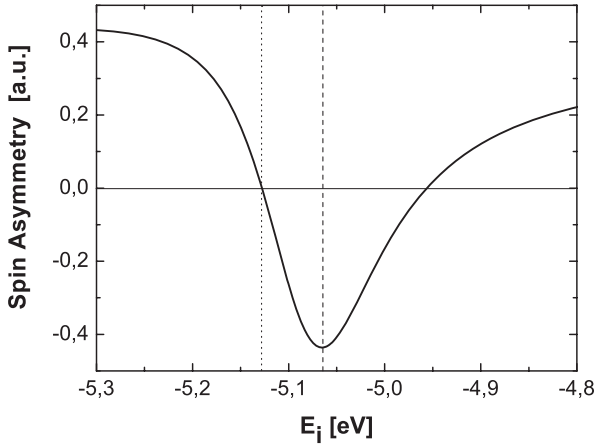

Figure 33. Spin asymmetry at the impurity location, at Fermi energy, calculated from figure 32.

has a resonance energy shifted from the STT resonance, it is not possible to increase both STT and TMR.

5. Resonant spin torque in a double tunnel barrier

5.1. Introduction

As stated in the introduction, Slonczewski predicted in 1989 that the magnetizations of two ferromagnetic layers separated by a thin tunnel barrier feel an interaction at zero bias voltage resulting from the transfer of spin associated with the symmetric tunnelling of spin-polarized electrons through the barrier [10]. Due to the relatively large critical current density required to observe spin transfer effects ($j_c \approx 10^7$ A cm^{-2}), it has long been believed that these phenomena could only be observed in metallic nanostructures. Indeed, magnetic tunnel junctions are

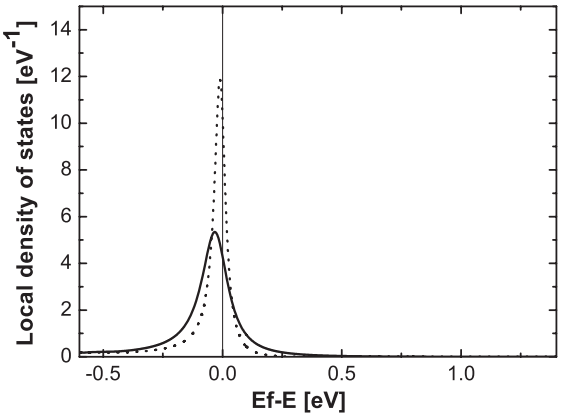

Figure 34. Spin-dependent local density of states at the IEC resonance versus electron energy for spin-up (solid line) and spin-down (dotted line).

voltage-limited since they undergo electrical breakdown when the barrier is exposed to too large a bias voltage (of the order of 1 V for a 1 nm thick barrier corresponding to a breakdown electrical field of the order of 10^9 V cm^{-1}).

Recently, thanks to progress in the development of low resistance tunnel barriers (resistance–area product below 10 Ω μm^2) with large TMR amplitude, some experimental groups have succeeded in observing spin torque effects in MTJ comparable to those observed in metallic spin-valve pillars [17–19]. The critical current density for switching in MTJ was found to be of the same order of magnitude (2×10^6–2×10^7 A cm^{-2}) as in their metallic counterparts. Various schemes are used to reduce the critical switching current density such as using magnetic material with lower magnetization (for instance CoFeB [19]), or by combining the effects of two reference layers in opposite magnetic states [18] as suggested by Berger [59].

In this section, we propose another approach to drastically enhance the spin torque efficiency based on the use of the resonant effect in double barrier magnetic tunnel junctions. The system we are interested in consists of a central free layer (F) sandwiched between two tunnel barriers (I_1 and I_2) themselves sandwiched between two ferromagnetic reference layers with in-plane magnetization (F_1 and F_2). In this geometry, the central free layer forms a spin-dependent quantum well. Under certain resonance conditions, we theoretically show that the electrical current as well as the spin current through the system can be drastically increased, yielding a correlative increase in the amplitude of the spin torque acting on the magnetization of the F layer.

5.2. Theoretical model

Our model system consists of two thick (semi-infinite) ferromagnetic electrodes (F_1 and F_2) connected to reservoirs with chemical potentials μ_1 and μ_2 and two non-magnetic insulating tunnel barriers (I_1 and I_2) of thickness b separated by a thin free ferromagnetic layer (F) of thickness a (see figure 35). The magnetizations of the outer electrodes are assumed to be pinned in-plane in either antiparallel or parallel alignment and the magnetization of the middle layer makes an angle θ with the direction of the F_1 magnetization supposed to be parallel to the z-axis. The x-axis is perpendicular to the plane of the layer. The y-axis is in plane, perpendicular to the x- and z-axes.

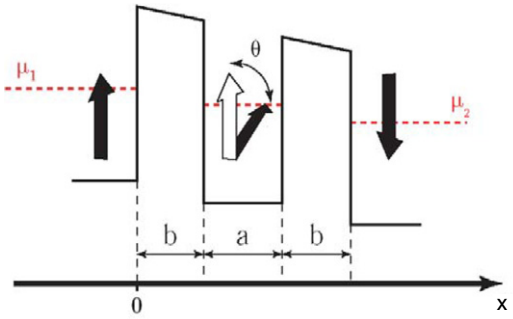

Figure 35. Schematic representation of energy potential seen by the tunnelling electrons in our model system.

(This figure is in colour only in the electronic version)

Using the s–d model (see section 4), the one-electron Hamiltonian of the system in layer α can be written in the following form:

$$H^{\alpha} = \left(\frac{\hat{p}^2(r)}{2m} - U^{\alpha}\right) - \sum_n J_{\mathrm{sd}}^{\alpha}(\mathbf{r} - \mathbf{R}_n)\left(\hat{\sigma}\hat{S}_n^{\alpha}\right) \tag{5.1}$$

where $\hat{p}(r)$ is the momentum operator of the conduction electron, J_{sd} is the s–d exchange constant, $\hat{\sigma}$ are Pauli matrices and $\hat{S}_n$ is the operator associated with the localized spin located at point $\mathbf{R}_n$ and responsible for the local magnetization. $J_{\mathrm{sd}}^{\alpha} = 0$ within the non-magnetic tunnel barriers and $J_{\mathrm{sd}}^{\alpha} \neq 0$ inside the ferromagnetic layers. $\alpha = 1, 2, \ldots, 5$ refers to the index of the layers, U^{α} represents the energy associated with the bottom of the conduction band in the ferromagnetic layers ($\alpha = 1, 3, 5$) and the height of the barriers in the insulating layers ($\alpha = 2, 4$). The ferromagnetic layers are assumed to be in single domain states. The two outer layers (F_1 and F_2) are in antiparallel (parallel) magnetic configuration whereas the magnetization of the central one makes an angle θ with the F_1 magnetization. The z-direction is chosen as the spin quantization axis for the two outer F layers and the Pauli matrix $\hat{\sigma}$ in the central layer with tilted magnetization ($\alpha = 3$) has to be transformed by the usual matrix of rotation

$$\hat{T} = \begin{bmatrix} \cos\frac{\theta}{2} & -\sin\frac{\theta}{2} \\ \sin\frac{\theta}{2} & \cos\frac{\theta}{2} \end{bmatrix}.$$

Finally, we consider that the electrons flowing from the left (right) reservoirs are represented by Fermi distributions with chemical potentials μ_1 (μ_2) so that $\mu_1 - \mu_2 = \mathrm{eV}$, where V is the applied voltage. A schematic picture of the potentials of the structure is shown in figure 35.

In order to calculate the electrical current and the components of the vectorial spin currents, we need to solve the Schrödinger equation and may use the expressions for the currents in terms of a transmission matrix (Landauer formalism), which is non-diagonal in spin-space in the case of non-collinear alignment of magnetizations in the ferromagnetic layers.

However, a more transparent way to calculate both currents and torques is to use the non-equilibrium Keldysh technique (as done in section 4), which allows us, in principle, to take into account elastic and inelastic processes of electron scattering. In the present section, elastic scattering in the F layer is not taken into account. In the rest of the section, we will use the mean field approximation for the operator $\hat{S}^{\alpha}$, so that $\hat{S}^{\alpha}$ is considered as a classical vector: ($S^z = S_0 \cos\theta$, $S^y = S_0 \sin\theta$, $S^x = 0$).

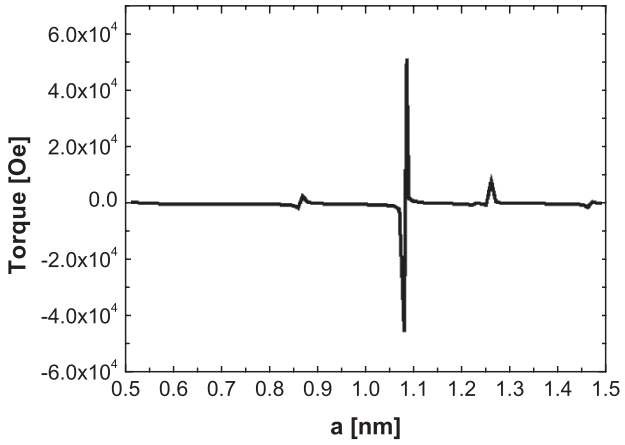

Figure 36. Torque calculated at a point of abscissa $x = 0.8$ nm located 0.1 nm from the I_1/F interface, as a function of the thickness a of the central F layer. The parameters used for the calculation were $k_F^{\uparrow} = 1.1$ Å^{-1}, $k_F^{\downarrow} = 0.6$ Å^{-1} in the F layer, $q_0 = 0.93$ Å^{-1} in the barrier, $b = 0.7$ nm. The outer electrodes were in antiparallel magnetic alignment.

In the case of an absence of scattering processes, the Keldysh Green functions can be calculated in the simple form:

$$G^{-+}(\mathbf{r},\mathbf{r}) = \begin{bmatrix} G^{-+}_{\uparrow\uparrow} & G^{-+}_{\uparrow\downarrow} \\ G^{-+}_{\downarrow\uparrow} & G^{-+}_{\downarrow\downarrow} \end{bmatrix} \tag{5.2}$$

where $G^{-+}_{\sigma\sigma'}(x,x')$ has the form of (4.3):

$$\begin{aligned} G^{-+}_{\sigma\sigma'}(x,x') = &\int_{\overrightarrow{K}} f_L \left(\Psi_L^{\sigma(\uparrow)}(x,\overrightarrow{\kappa}) \Psi_L^{*\sigma'(\uparrow)}(x',\overrightarrow{\kappa}) + \Psi_L^{\sigma(\downarrow)}(x,\overrightarrow{\kappa}) \Psi_L^{*\sigma'(\downarrow)}(x',\overrightarrow{\kappa}) \right) \mathrm{d}\overrightarrow{\kappa} \\ &+ \int_{\overrightarrow{K}} f_R \left(\Psi_R^{\sigma(\uparrow)}(x,\overrightarrow{\kappa}) \Psi_R^{*\sigma'(\uparrow)}(x',\overrightarrow{\kappa}) + \Psi_R^{\sigma(\downarrow)}(x,\overrightarrow{\kappa}) \Psi_R^{*\sigma'(\downarrow)}(x',\overrightarrow{\kappa}) \right) \mathrm{d}\overrightarrow{\kappa} \end{aligned} \tag{5.3}$$

where f_L (respectively f_R) are the Fermi distribution functions for the left (respectively right) reservoir, $\Psi^{\sigma(\alpha)}_{L(R)}(x,\overrightarrow{\kappa})$ is the spinor (index σ) wavefunction of the electron when an electron with spin α, energy E and momentum $\overrightarrow{\kappa}$ in the yz-plane is injected from the left (right) reservoir. We point out that for non-collinear alignment of the magnetizations in the ferromagnetic layers, the indices σ and α may not coincide. This means that an electron with an initial spin index $\alpha = \uparrow$ (for example) undergoing partial reflection and partial penetration into the F layer reaches an entangled state in which neither $\uparrow$ and $\downarrow$ components are equal to 0. The system of wavefunctions $\psi^{\sigma(\alpha)}_{L(R)}(x,\kappa)$ is a full and orthogonal system of eigenfunctions. The latter are normalized to the unit flow.

The currents and non-equilibrium magnetization can be calculated using the expressions (4.10), (4.11) and (4.12). The wavefunctions $\psi^{\sigma(\alpha)}_{L(R)}(x,\overrightarrow{\kappa})$ are determined from (5.1) following the same procedure as in section 4.

Equation (5.3) clearly shows that the torque is an oscillatory function of the distance from the I/F interface. This will be further illustrated below. In figure 36, the dependence of the local torque on the thickness of the central ferromagnetic layer F is plotted at a particular location in the middle layer (point of abscissa $a = 0.8$ nm located 0.1 nm from the I_1/F interface). The parameters used for the spin-dependent Fermi momenta in the ferromagnetic

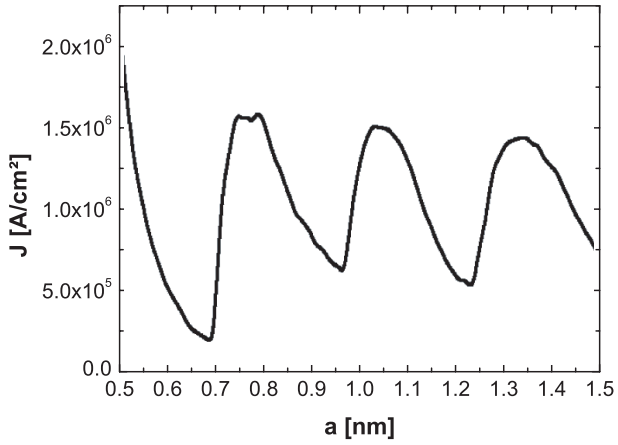

Figure 37. Total charge current through the system as a function of the thickness of the central F layer. The parameters were the same as in figure 36.

layers are representative of the case of Ni ($k_{\mathrm{F}}^{\uparrow} = 1.1$ Å^{-1}, $k_{\mathrm{F}}^{\uparrow} = 0.6$ Å^{-1}). The damping vector in the tunnel barrier is reasonable for alumina barriers ($q_0 = 0.93$ Å^{-1}). The calculation was performed assuming antiparallel alignment of the magnetization of the outer layers. The torque amplitude is expressed as the effective field (H_{eff} in Oe) in (4.14). Very sharp peaks in torque amplitude are observed with amplitudes exceeding 5×10^4 Oe. For comparison, in a single barrier tunnel junction using the same parameters for the barrier and the F layer, the spin torque amplitude at the same location would be only 200 Oe. However, these peaks occur over an extremely narrow range of thickness corresponding to particular resonance conditions. In materials such as magnetic semiconductors in which the Fermi wavelengths are much longer than in transition metals (by two orders of magnitude), the peaks would occur over much broader ranges of thickness.

Alternatively, with a transition metal, one way to reach the resonance condition could consist in changing the Fermi momenta by adding non-magnetic impurities within the ferromagnetic metal (Cu impurities introduced in Ni or NiFe for instance). The reason for such high values is the resonant character of the torque and current for some definite values of the middle layer thickness. This resonance character also shows up in the variation of the charge current (i.e. the conductance of the system) as a function of the thickness of the central F layer (see figure 37). A clear oscillatory behaviour is observed. The current has resonances at values of the thickness a approximately equal $k_{\mathrm{F}}^{\uparrow} a = 2\pi n + \phi_0$. The torque (figure 36) has resonances at points a slightly shifted from the location of the resonances in the current. The resonances in torque are much sharper than the oscillations of the current and they have the form of a dispersion curve. Such behaviour may be explained by the fact that the four contributions to the torque (see expression (5.3)) have different signs and exhibit some shifts in the phase. This may be understood by considering that the contributions to the torque of electrons with different spin or momentum directions have different signs.

Figure 38 shows the variation of the spin torque amplitude versus location along the x-axis within the free central layer. The calculation was performed at conditions corresponding to a resonance of the spin torque. It is interesting to note that in the resonance conditions, the spatial variation of the torque is symmetric (left-right) within the free layer both in parallel and antiparallel alignment of the magnetization in the outer electrodes. The average value of the torque over the total thickness of the layer is not zero in antiparallel alignment but ≈900 Oe.

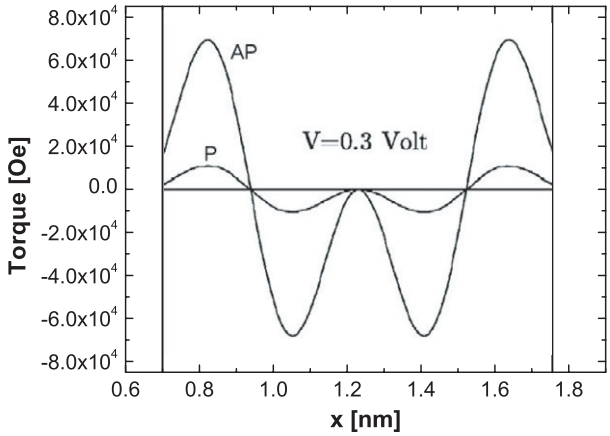

Figure 38. Local variation of the torque amplitude versus location along the x-axis in the middle free layer for parallel and antiparallel alignment of the magnetization in the two outer pinned electrodes. The calculation is performed in resonance conditions ($a = 1.06$ nm, $V = 0.3$ V and for the same parameters as in figure 36). Note that at resonance, the torque exhibits a symmetric profile within the free layer.

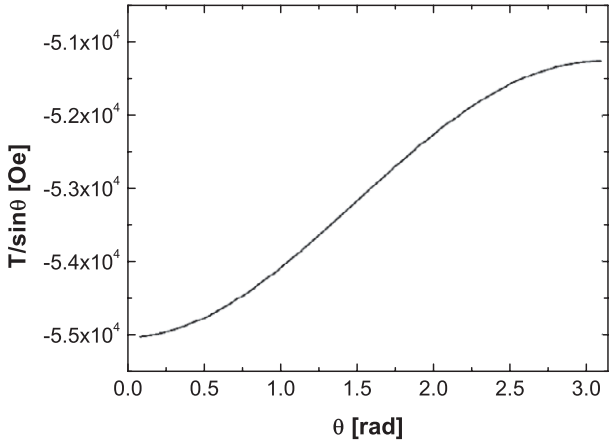

Figure 39. Angular variation of the torque normalized by $\sin\theta$ where θ is the angle between the magnetization in the outer electrodes (supposed to be antiparallel) and the magnetization of the free layer. The parameters used in the calculation were the same as in figure 36.

Furthermore, we investigated the dependence of the spin torque on the angle θ between the magnetization in the free layer and in the outer magnetic electrodes supposed to be in antiparallel magnetic alignment. Figure 39 shows the angular variation of the torque divided by $\sin\theta$. A clear deviation from a constant value is observed as already discussed by other authors [20].

6. Conclusion

As an introduction, we defined microscopically the spin transfer torque and current-driven exchange coupling as being proportional to the transverse component of the effective local magnetization, or spin accumulation. We applied this definition to three different kinds of structure: metallic spin-valve, magnetic tunnel junction and double magnetic tunnel junction.

We first proposed a universal model allowing the calculation of currents and torques in any kind of metallic multilayered structure, for any kind of magnetization orientation. We showed that the angular dependences of spin torque and normalized stack resistance are of the same nature, which means that spin torque and magnetoresistance originate from the same physical phenomenon, as suggested by recent experiments [60].

In a second step, we proposed a thorough study of spin torque and interlayer exchange coupling in a magnetic tunnel junction with an amorphous barrier. We find that the averaged spin torque and interlayer exchange coupling oscillate with the thickness of the layer. This model also gives an important asymmetry in spin torque, as suggested by Slonczewski [21]. Finally, we showed that the interlayer exchange coupling can be of the same order as spin torque in MTJ, depending on the barrier characteristics.

We then showed that introducing a layer of impurities inside the barrier induces spin-dependent resonance states yielding a great enhancement of spin torque and interlayer exchange coupling. The IEC also shows an inversion depending on the impurity energy and location, as discussed in [49].

Finally, we proposed another way to increase spin torque, using double magnetic tunnel junctions. We showed that a dramatic enhancement in spin torque amplitude can be obtained in double junction systems when resonance conditions in the central free layer are fulfilled.

Acknowledgments

The authors acknowledge Professors John Slonczewski and Albert Fert for very fruitful discussions. The work and results reported were partly obtained with research funding from the European Community under the sixth Framework, contract number 510993: MAGLOG. The views expressed are solely those of the authors, and the other contractors and/or the European Community cannot be held liable for any use that may be made of the information contained herein. Professor A Vedyayev, N Ryzhanova and N Strelkov acknowledge CEA and CNRS for fellowships. This work was partially financially supported by the Russian Fund for Basic Research (grant no 04-02-166888-a) and the French ACI program CALOMAG.

Appendix A. Diffusion coefficients

The matrix $\hat{A}_n$ has the following structure:

$$A_{n11} = A_{n12} = A_{n13} = A_{n14} = \frac{\gamma_n^x \cos\Theta_n - \gamma_n^z \sin\Theta_n}{r_n}$$

$$A_{n15} = A_{n16} = \frac{1}{r_n}\left[\left(\gamma_n^x \sin\Theta_n + \gamma_n^z \cos\Theta_n\right)(1 + \beta_n'\delta_n) - (\beta_n' + \delta_n)\right]$$

$$A_{n17} = \frac{1}{r_n}\left[1 - \delta_n\left(\gamma_n^x \sin\Theta_n + \gamma_n^z \cos\Theta_n\right)\right]$$

$$A_{n21} = A_{n22} = A_{n23} = A_{n24} = \frac{\cos\Theta_n}{r_n}$$

$$A_{n25} = A_{n26} = \frac{1}{r_n}\left[\sin\Theta_n(1 + \beta_n'\delta_n) - \gamma_n^x(\beta_n' + \delta_n)\right]$$

$$A_{n27} = \frac{1}{r_n}\left(\gamma_n^x - \delta_n \sin\Theta_n\right)$$

$$A_{n31} = A_{n32} = A_{n33} = A_{n34} = \frac{\mathrm{i}}{r_n}$$

$$
\begin{aligned}
A_{n35} &= A_{n36} = A_{n37} = 0\\
A_{n41} &= A_{n42} = A_{n43} = A_{n44} = -\frac{\sin\Theta_n}{r_n}\\
A_{n45} &= A_{n46} = \frac{1}{r_n}\left[\cos\Theta_n(1+\beta'_n\delta_n) - \gamma_n^z(\beta'_n+\delta_n)\right]\\
A_{n47} &= \frac{\gamma_n^z - \delta_n\cos\Theta_n}{r_n}\\
A_{n51} &= -A_{n52} = -\cos\Theta_{n+1}k_{n+11}\frac{1-\beta_{n+1}\delta_{n+1}}{\rho_n}\\
A_{n53} &= -A_{n54} = -\cos\Theta_{n+1}k_{n+12}\frac{1-\beta_{n+1}\delta_{n+1}}{\rho_n+1}\\
A_{n55} &= -A_{n56} = \sin\Theta_{n+1}k_{n+13}\left(\beta'^2_{n+1}-1\right)\frac{1-\beta_{n+1}\delta_{n+1}}{\rho_{n+1}}\\
A_{n57} &= 0\\
A_{n61} &= -A_{n62} = -\mathrm{i}k_{n+11}\frac{1-\beta_{n+1}\delta_{n+1}}{\rho_{n+1}}\\
A_{n63} &= -A_{n64} = -\mathrm{i}k_{n+12}\frac{1-\beta_{n+1}\delta_{n+1}}{\rho_{n+1}}\\
A_{n65} &= A_{n66} = A_{n67} = 0\\
A_{n71} &= -A_{n72} = \sin\Theta_{n+1}k_{n+11}\frac{1-\beta_{n+1}\delta_{n+1}}{\rho_{n+1}}\\
A_{n73} &= -A_{n74} = \sin\Theta_{n+1}k_{n+12}\frac{1-\beta_{n+1}\delta_{n+1}}{\rho_{n+1}}\\
A_{n75} &= A_{n76} = \cos\Theta_{n+1}k_{n+13}\left(\beta'^2_{n+1}-1\right)\frac{1-\beta_{n+1}\delta_{n+1}}{\rho_{n+1}}\\
A_{n77} &= 0.
\end{aligned}
$$

The matrix $\hat{B}_n$ has a similar structure:

$$
\begin{aligned}
B_{n11} &= B_{n12} = \frac{\mathrm{e}^{k_{n1}t_n}}{r_n}\left(\gamma_n^x\cos\Theta_n - \gamma_n^z\sin\Theta_n\right)\\
B_{n13} &= B_{n14} = \frac{\mathrm{e}^{k_{n2}t_n}}{r_n}\left(\gamma_n^x\cos\Theta_n - \gamma_n^z\sin\Theta_n\right)\\
B_{n15} &= B_{n16} = \frac{\mathrm{e}^{k_{n3}t_n}}{r_n}\left[\left(\gamma_n^x\sin\Theta_n - \gamma_n^z\cos\Theta_n\right)\left(1+\beta'_n\delta_n\right) - \left(\beta'_n+\delta_n\right)\right]\\
B_{n17} &= \frac{1}{r_n}\left[1-\delta_n\left(\gamma_n^x\sin\Theta_n + \gamma_n^z\cos\Theta_n\right)\right]\\
B_{n21} &= \mathrm{e}^{kn1t_n}\cos\Theta_n\left(\frac{1}{r_n} + k_{n1}\frac{1-\beta_n\delta_n}{\rho_n}\right)\\
B_{n22} &= \mathrm{e}^{-kn1t_n}\cos\Theta_n\left(\frac{1}{r_n} - k_{n1}\frac{1-\beta_n\delta_n}{\rho_n}\right)\\
B_{n23} &= \mathrm{e}^{kn2t_n}\cos\Theta_n\left(\frac{1}{r_n} + k_{n2}\frac{1-\beta_n\delta_n}{\rho_n}\right)\\
B_{n24} &= \mathrm{e}^{-kn2t_n}\cos\Theta_n\left(\frac{1}{r_n} - k_{n2}\frac{1-\beta_n\delta_n}{\rho_n}\right)
\end{aligned}
$$

$$B_{n25} = \mathrm{e}^{k_{n3}t_n}\left\{\frac{1}{r_n}\left[\sin\Theta_n\left(1+\beta'_n\delta_n\right)-\gamma_n^x\left(\beta'_n+\delta_n\right)\right]-k_{n3}\sin\Theta_n\left(\beta_n'^2-1\right)\frac{1-\beta_n\delta_n}{\rho_n}\right\}$$

$$B_{n26} = \mathrm{e}^{-k_{n3}t_n}\left\{\frac{1}{r_n}\left[\sin\Theta_n\left(1+\beta'_n\delta_n\right)+\gamma_n^x\left(\beta'_n+\delta_n\right)\right]+k_{n3}\sin\Theta_n\left(\beta_n'^2-1\right)\frac{1-\beta_n\delta_n}{\rho_n}\right\}$$

$$B_{n27} = \frac{1}{r_n}\left(\gamma_n^x-\delta_n\sin\theta_n\right)$$

$$B_{n31} = \mathrm{i}\mathrm{e}^{kn1t_n}\left(\frac{1}{r_n}+k_{n1}\frac{1-\beta_n\delta_n}{\rho_n}\right)$$

$$B_{n32} = \mathrm{i}\mathrm{e}^{-kn1t_n}\left(\frac{1}{r_n}-k_{n1}\frac{1-\beta_n\delta_n}{\rho_n}\right)$$

$$B_{n33} = -\mathrm{i}\mathrm{e}^{kn2t_n}\left(\frac{1}{r_n}+k_{n2}\frac{1-\beta_n\delta_n}{\rho_n}\right)$$

$$B_{n34} = -\mathrm{i}\mathrm{e}^{kn2t_n}\left(\frac{1}{r_n}-k_{n2}\frac{1-\beta_n\delta_n}{\rho_n}\right)$$

$$B_{n35} = B_{n36} = B_{n37} = 0$$

$$B_{n41} = -\mathrm{e}^{kn1t_n}\sin\Theta_n\left(\frac{1}{r_n}+k_{n1}\frac{1-\beta_n\delta_n}{\rho_n}\right)$$

$$B_{n42} = -\mathrm{e}^{-kn1t_n}\sin\Theta_n\left(\frac{1}{r_n}-k_{n1}\frac{1-\beta_n\delta_n}{\rho_n}\right)$$

$$B_{n43} = -\mathrm{e}^{kn2t_n}\sin\Theta_n\left(\frac{1}{r_n}+k_{n2}\frac{1-\beta_n\delta_n}{\rho_n}\right)$$

$$B_{n44} = -\mathrm{e}^{-kn2t_n}\sin\Theta_n\left(\frac{1}{r_n}-k_{n2}\frac{1-\beta_n\delta_n}{\rho_n}\right)$$

$$B_{n45} = \mathrm{e}^{k_{n3}t_n}\left\{\frac{1}{r_n}\left[\cos\Theta_n\left(1+\beta'_n\delta_n\right)-\gamma_n^z\left(\beta'_n+\delta_n\right)\right]-k_{n3}\cos\Theta_n\left(\beta_n'^2-1\right)\frac{1-\beta_n\delta_n}{\rho_n}\right\}$$

$$B_{n46} = \mathrm{e}^{k_{n3}t_n}\left\{\frac{1}{r_n}\left[\cos\Theta_n\left(1+\beta'_n\delta_n\right)-\gamma_n^z\left(\beta'_n+\delta_n\right)\right]+k_{n3}\cos\Theta_n\left(\beta_n'^2-1\right)\frac{1-\beta_n\delta_n}{\rho_n}\right\}$$

$$B_{n47} = \frac{1}{r_n}\left(\gamma_n^z-\delta_n\cos\Theta_n\right)$$

$$B_{nij} = A_{nij}\ (n+1\Rightarrow n)$$

$$\hat{R}_n = \begin{bmatrix} c_{n8}\left\{\frac{t_n}{r_n}\left[1-\delta_n\left(\gamma_n^x\sin\Theta_n+\gamma_n^z\cos\Theta_n\right)\right]-\frac{1-\beta_n\delta_n}{\rho_n}\right\}-\frac{E_x}{2\rho_n} \\ c_{n8}\left[\sin\Theta_n\beta'_n\frac{1-\beta_n\delta_n}{\rho_n}+t_n\frac{\gamma_n^x-\delta_n\sin\Theta_n}{r_n}\right]-\frac{\beta_n\sin\Theta_nE_x}{2\rho_n} \\ c_{n8}\left[\cos\Theta_n\beta'_n\frac{1-\beta_n\delta_n}{\rho_n}+t_n\frac{\gamma_n^z-\delta_n\cos\Theta_n}{r_n}\right]-\frac{\beta_n\cos\Theta_nE_x}{2\rho_n} \\ \frac{\sin\Theta_n}{\rho_n}\left[\frac{\beta_nE_x}{2}-c_{n8}\beta'_n\left(-1\beta_n\delta_n\right)\right]-\frac{\sin\Theta_{n+1}}{\rho_{n+1}}\left[\frac{\beta_{n+1}E_x}{2}-c_{n+18}\beta'_{n+1}\left(1-\beta_{n+1}\delta_{n+1}\right)\right] \\ \frac{\cos\Theta_n}{\rho_n}\left[\frac{\beta_nE_x}{2}-c_{n8}\beta'_n\left(-1\beta_n\delta_n\right)\right]-\frac{\cos\Theta_{n+1}}{\rho_{n+1}}\left[\frac{\beta_{n+1}E_x}{2}-c_{n+18}\beta'_{n+1}\left(1-\beta_{n+1}\delta_{n+1}\right)\right] \end{bmatrix}$$

where $t_n = x_{n+1} - x_n$ is the thickness of the nth layer.

Appendix B. Spin-dependent wavefunctions in a clean MTJ

Some functions which will be used in the description of the wavefunctions are first defined:

$$q_0^2 = \frac{2m}{\hbar^2}(U - E_F)$$

$$q(x) = \sqrt{q_0^2 - \frac{2m}{\hbar^2}\left(\frac{x - x_1}{x_2 - x_1}eV - \epsilon\right) + \kappa^2}$$

$$q_1 = q(x_1)$$

$$q_2 = q(x_2)$$

$$k_{1(2)} = \sqrt{\left(k_F^{\uparrow(\downarrow)}\right)^2 - \frac{2m}{\hbar^2}\epsilon - \kappa^2}$$

$$k_{3(4)} = \sqrt{\left(k_F^{\uparrow(\downarrow)}\right)^2 - \frac{2m}{\hbar^2}(\epsilon - eV) - \kappa^2}$$

$$E(x_i, x_j) = \exp\int_{x_i}^{x_j} q(x)\,\mathrm{d}x$$

$$E_n = E(x_1, x_2)$$

where E_F is the Fermi energy, U is the height of the barrier, V is the bias voltage and $\epsilon = E_F - E$, E being the energy of the tunnelling electron. We define:

$$\Psi(q_1, k_i, q_2, k_j) = E_n(q_1 - \mathrm{i}k_i)(q_2 - \mathrm{i}k_j) - E_n^{-1}(q_1 + \mathrm{i}k_i)(q_2 + \mathrm{i}k_j)$$

$$\phi(q_1, k_i, q_2, k_j) = E_n(q_1 + \mathrm{i}k_i)(q_2 - \mathrm{i}k_j) - E_n^{-1}(q_1 - \mathrm{i}k_i)(q_2 + \mathrm{i}k_j)$$

$$\begin{aligned}\mathrm{Den} = {} & \Psi(q_1, k_1, q_2, k_3)\Psi(q_1, k_2, q_2, k_4)(1 + \cos\theta) \\ & + \Psi(q_1, k_2, q_2, k_3)\Psi(q_1, k_1, q_2, k_4)(1 - \cos\theta)\end{aligned}$$

$$\begin{aligned}r_1^{\uparrow} = \frac{1}{\mathrm{Den}}[& \phi(q_1, k_1, q_2, k_3)\Psi(q_1, k_2, q_2, k_4)(1 + \cos\theta) \\ & + \phi(q_1, k_1, q_2, k_4)\Psi(q_1, k_2, q_2, k_3)(1 - \cos\theta)]\end{aligned}$$

$$\begin{aligned}r_3^{\uparrow} = \frac{1}{\mathrm{Den}}[& \phi(q_2, k_3, q_1, k_1)\Psi(q_1, k_2, q_2, k_4)(1 + \cos\theta) \\ & + \phi(q_2, k_3, q_1, k_2)\Psi(q_1, k_1, q_2, k_4)(1 - \cos\theta)].\end{aligned}$$

Electrons originally in the left electrode have the following wavefunctions along the structure:

$$\Psi_L^{\uparrow(\uparrow)}(-\infty < x < x_1) = \frac{1}{\sqrt{k_1}}\left[\mathrm{e}^{\mathrm{i}k_1(x - x_1)} - r_1^{\uparrow}\mathrm{e}^{-\mathrm{i}k_1(x - x_1)}\right]$$

$$\Psi_L^{\downarrow(\uparrow)}(-\infty < x < x_1) = \frac{8q_1q_2\sqrt{k_1}(k_3 - k_4)\sin\theta}{\mathrm{Den}}\mathrm{e}^{-\mathrm{i}k_2(x - x_1)}$$

$$\begin{aligned}\Psi_L^{\uparrow(\uparrow)}(x_1 < x < x_2) = {} & \frac{2}{\mathrm{iDen}}\sqrt{\frac{k_1q_1}{q(x)}}\big\{E(x_2, x)\big[\Psi(q_1, k_2, q_2, k_4)(q_2 + \mathrm{i}k_3)(1 + \cos\theta) \\ & + \Psi(q_1, k_2, q_2, k_3)(q_2 + \mathrm{i}k_4)(1 - \cos\theta)\big] \\ & + E^{-1}(x_2, x)[\Psi(q_1, k_2, q_2, k_4)(q_2 - \mathrm{i}k_3)(1 + \cos\theta) \\ & + \Psi(q_1, k_2, q_2, k_3)(q_2 - \mathrm{i}k_4)(1 - \cos\theta)]\big\}\end{aligned}$$

$$\Psi_L^{\downarrow(\uparrow)}(x_1 < x < x_2)$$
$$= \frac{4q_2}{\mathrm{Den}}\sqrt{\frac{k_1 q_1}{q(x)}}(k_3 - k_4)\sin\theta\left[E(x_1,x)(q_1 - \mathrm{i}k_2) + E^{-1}(x_1,x)(q_1 + \mathrm{i}k_2)\right]$$

$$\Psi_L^{\uparrow(\uparrow)}(x_2 < x < \infty) = \frac{4}{\mathrm{iDen}}\sqrt{k_1 q_1 q_2}\left[\mathrm{e}^{\mathrm{i}k_3(x-x_2)}\Psi(q_1,k_2,q_2,k_4)(1+\cos\theta)\right.$$
$$\left. + \mathrm{e}^{\mathrm{i}k_4(x-x_2)}\Psi(q_1,k_2,q_2,k_3)(1-\cos\theta)\right]$$

$$\Psi_L^{\downarrow(\uparrow)}(x_2 < x < \infty)$$
$$= \frac{4}{\mathrm{iDen}}\sqrt{k_1 q_1 q_2}\left[\mathrm{e}^{\mathrm{i}k_3(x-x_2)}\Psi(q_1,k_2,q_2,k_4) - \mathrm{e}^{\mathrm{i}k_4(x-x_2)}\Psi(q_1,k_2,q_2,k_3)\right]\sin\theta.$$

Electrons originally in the right electrode have the following wavefunctions along the structure:

$$\Psi_R^{\uparrow(\uparrow)}(-\infty < x < x_1) = \frac{8}{\mathrm{iDen}}\sqrt{q_1 q_2 k_3}\Psi(q_1,k_2,q_2,k_4)\cos\frac{\theta}{2}\mathrm{e}^{-\mathrm{i}k_1(x-x_1)}$$

$$\Psi_R^{\downarrow(\uparrow)}(-\infty < x < x_1) = \frac{8}{\mathrm{iDen}}\sqrt{q_1 q_2 k_3}\Psi(q_1,k_1,q_2,k_4)\sin\frac{\theta}{2}\mathrm{e}^{-\mathrm{i}k_2(x-x_1)}$$

$$\Psi_R^{\uparrow(\uparrow)}(x_1 < x < x_2) = \frac{4}{\mathrm{iDen}}\sqrt{\frac{k_3 q_2}{q(x)}}\Psi(q_1,k_2,q_2,k_4)$$
$$\times\ \cos\frac{\theta}{2}\left[E(x_1,x)(q_1 - \mathrm{i}k_1) + E^{-1}(x_1,x)(q_1 + \mathrm{i}k_1)\right]$$

$$\Psi_R^{\downarrow(\uparrow)}(x_1 < x < x_2) = \frac{4}{\mathrm{iDen}}\sqrt{\frac{k_3 q_2}{q(x)}}\Psi(q_1,k_1,q_2,k_4)$$
$$\times\ \sin\frac{\theta}{2}\left[E(x_1,x)(q_1 - \mathrm{i}k_2) + E^{-1}(x_1,x)(q_1 + \mathrm{i}k_2)\right]$$

$$\Psi_R^{\uparrow(\uparrow)}(x_2 < x < \infty) = \cos\frac{\theta}{2}\frac{1}{\sqrt{k_3}}\left[\mathrm{e}^{-\mathrm{i}k_3(x-x_2)} - r_3^{\uparrow}\mathrm{e}^{\mathrm{i}k_3(x-x_2)}\right]$$
$$+\ \sin\frac{\theta}{2}\frac{\sin\theta}{\sqrt{k_3}}\frac{8q_1q_2k_3(k_1-k_2)}{\mathrm{Den}}\mathrm{e}^{\mathrm{i}k_4(x-x_2)}$$

$$\Psi_R^{\downarrow(\uparrow)}(x_2 < x < \infty) = \sin\frac{\theta}{2}\frac{1}{\sqrt{k_3}}\left[\mathrm{e}^{-\mathrm{i}k_3(x-x_2)} - r_3^{\uparrow}\mathrm{e}^{\mathrm{i}k_3(x-x_2)}\right]$$
$$-\ \cos\frac{\theta}{2}\frac{\sin\theta}{\sqrt{k_3}}\frac{8q_1q_2k_3(k_1-k_2)}{\mathrm{Den}}\mathrm{e}^{\mathrm{i}k_4(x-x_2)}.$$

To obtain $\Psi^{\downarrow(\downarrow)}$ and $\Psi^{\uparrow(\downarrow)}$ from $\Psi^{\uparrow(\uparrow)}$ and $\Psi^{\downarrow(\uparrow)}$, θ must be replaced by $-\theta$ and k_1 (k_3) by k_2 (k_4) in the above formulae.

Appendix C. Equilibrium Green functions

We only give here the Green functions which appear in appendix D. Advanced Green functions G^A are the conjugated complexes of retarded Green functions G^R.

$$G^R_{0\uparrow\uparrow}(x_0,x) = -\frac{\mathrm{e}^{\mathrm{i}k_1(x-x_1)}}{\mathrm{Den}}\sqrt{\frac{q_1}{q(x_0)}}\left\{E(x_2,x_0)\left[\Psi(q_1,k_2,q_2,k_3)(q_2+\mathrm{i}k_4)(1-\cos\theta)\right.\right.$$
$$\left.\left. + \Psi(q_1,k_2,q_2,k_4)(q_2+\mathrm{i}k_3)(1+\cos\theta)\right]\right.$$

$$
\begin{aligned}
&+ E^{-1}(x_2, x_0)[\Psi(q_1, k_2, q_2, k_3)(q_2 - \mathrm{i}k_4)(1 - \cos\theta) \\
&+ \Psi(q_1, k_2, q_2, k_4)(q_2 - \mathrm{i}k_3)(1 + \cos\theta)]\Big\} = G^R_{0\uparrow\uparrow}(x, x_0) \\
G^R_{0\downarrow\uparrow}(x_0, x) &= \frac{2\sin\theta(k_3 - k_4)q_2}{\mathrm{iDen}} \mathrm{e}^{-\mathrm{i}k_1(x - x_1)} \\
&\times \sqrt{\frac{q_1}{q(x_0)}}\{E(x_1, x_0)(q_1 - \mathrm{i}k_2) + E^{-1}(x_1, x_0)(q_1 + \mathrm{i}k_2)\} = G^R_{0\uparrow\downarrow}(x, x_0) \\
G^R_{0\uparrow\uparrow}(x_0, x_0) &= -\frac{1}{2\mathrm{Den}q(x_0)}\{E(x_2, x_0)[\Psi(q_1, k_2, q_2, k_3)(q_2 + \mathrm{i}k_4)(1 - \cos\theta) \\
&+ \Psi(q_1, k_2, q_2, k_4)(q_2 + \mathrm{i}k_3)(1 + \cos\theta)] \\
&+ E^{-1}(x_2, x_0)[\Psi(q_1, k_2, q_2, k_3)(q_2 - \mathrm{i}k_4)(1 - \cos\theta) \\
&+ \Psi(q_1, k_2, q_2, k_4)(q_2 - \mathrm{i}k_3)(1 + \cos\theta)]\} \\
&\times \{E(x_1, x_0)(q_1 - \mathrm{i}k_1) + E^{-1}(x_1, x_0)(q_1 + \mathrm{i}k_1)\} \\
G^R_{0\downarrow\uparrow}(x_0, x_0) &= \frac{\sin\theta(k_3 - k_4)}{2\mathrm{iDen}q(x_0)}\left[E(x_1, x_0)(q_1 - \mathrm{i}k_2) + E^{-1}(x_1, x_0)(q_1 + \mathrm{i}k_2)\right] \\
&\times \left[E(x_1, x_0)(q_1 - \mathrm{i}k_1) + E^{-1}(x_1, x_0)(q_1 + \mathrm{i}k_1)\right].
\end{aligned}
$$

To obtain the $G^R_{0\uparrow\downarrow}$ from $G^R_{0\downarrow\uparrow}$, we must replace k_1 (k_3) by k_2 (k_4) and θ by $-\theta$. To obtain the $G^R_{0\downarrow\downarrow}$ from $G^R_{0\uparrow\uparrow}$, we must replace k_1 (k_3) by k_2 (k_4) only.

Appendix D. Out of equilibrium Green functions

The non-equilibrium advanced Green functions are the complex conjugates of non-equilibrium retarded Green functions. Advanced Green functions have the following expressions:

$$
\begin{aligned}
G^A_{\uparrow\uparrow}(x_0, x) &= \frac{1}{\mathrm{Den}*}\{G^A_{0\uparrow\uparrow}(x_0, x)\left(1 - WG^A_{0\downarrow\downarrow}(r_0, r_0)\right) + WG^A_{0\uparrow\downarrow}(r_0, r_0)G^A_{0\downarrow\uparrow}(x_0, x)\} \\
G^A_{\downarrow\uparrow}(x_0, x) &= \frac{1}{\mathrm{Den}*}\{G^A_{0\downarrow\uparrow}(x_0, x)\left(1 - WG^A_{0\uparrow\uparrow}(r_0, r_0)\right) + WG^A_{0\downarrow\uparrow}(r_0, r_0)G^A_{0\uparrow\uparrow}(x_0, x)\} \\
\mathrm{Den} &= \left[1 - WG^R_{0\uparrow\uparrow}(r_0, r_0)\right]\left[1 - WG^R_{0\downarrow\downarrow}(r_0, r_0)\right] - W^2G^R_{0\uparrow\downarrow}(r_0, r_0)G^R_{0\downarrow\uparrow}(r_0, r_0) \\
G^\alpha_{\sigma\sigma'}(\mathbf{r}_0, \mathbf{r}_0) &= \frac{a_0^2}{2\pi}\int_0^{2\sqrt{\pi}/a_0} G^\alpha_{\sigma\sigma',\kappa}(x_0, x_0)\kappa\,\mathrm{d}\kappa.
\end{aligned}
$$

The other non-equilibrium Green functions are obtained symmetrically. Den$*$ signify integration over κ of Den.

References

[1] Bass J and Pratt W P Jr 1999 *J. Magn. Magn. Mater.* **200** 274

[2] Tsymbal E Y, Mryasov O N and LeClair P R 2003 *J. Phys.: Condens. Matter* **15** R109

[3] Baibich M N, Broto J M, Fert A, Nguyen Van Dau F, Petroff F, Eitenne P, Creuzet G, Friedrerich A and Chazelas J 1988 *Phys. Rev. Lett.* **61** 2472
Dieny B, Speriosu V S, Parkin S S P, Gurney B A, Wilhoit D R and Mauri D 1991 *Phys. Rev.* B **43** 1297

[4] Moodera J S, Kinder L R, Wong T M and Meservey R 1995 *Phys. Rev. Lett.* **74** 3273

[5] Gregg J F, Petej I, Jouguelet E and Dennis C 2002 *J. Phys. D: Appl. Phys.* **35** R121

[6] Everitt B A, Olson D, van Nguyen T, Amin N, Pokhil T, Kolbo P, Zhong L, Murdock E, Pohm A V and Daughton J M 2005 *IEEE Trans. Magn.* **41** 125

[7] Slonczewski J C 1997 *US Patent* 5,695,864
Redon O, Dieny B and Rodmacq B 2003 *US Patent* 6,532,164 B2

[8] Koh G H *et al* 2004 *J. Magn. Magn. Mater.* **272** 1941
[9] Fert A *et al* 2001 *Mater. Sci. Eng.* B **84** 1
[10] Slonczewski J C 1989 *Phys. Rev.* B **39** 6995
[11] Slonczewski J C 1996 *J. Magn. Magn. Mater.* **159** L1
[12] Berger L 1996 *Phys. Rev.* B **54** 9353
[13] Tsoi M, Jansen A G M, Bass J, Chiang W C, Seck M, Tsoi V and Wyder P 1998 *Phys. Rev. Lett.* **80** 4281
Tsoi M, Jansen A G M, Bass J, Chiang W C, Tsoi V and Wyder Pr 2000 *Nature* **406** 46
[14] Katine J A, Albert F J, Buhrman R A, Myers E B and Ralph D C 2000 *Phys. Rev. Lett.* **84** 3149
[15] Kiselev S I *et al* 2003 *Phys. Rev. Lett.* **93** 036601
[16] Rippard W H, Pufall M R, Kaka S, Silva T J and Russek S E 2004 *Phys. Rev.* B **70** 100406
[17] Huai Y, Albert F, Nguyen P, Pakala M and Valet T 2004 *Appl. Phys. Lett.* **84** 3118
[18] Fuchs G D, Emley N C, Krivorotov I N, Braganca P M, Ryan E M, Kiselev S I, Sankey J C, Ralph D C, Buhrman R A and Katine J A 2004 *Appl. Phys. Lett.* **85** 1205
Fuchs G D, Krivorotov I N, Braganca P M, Emley N C, Garcia A G F, Ralph D C and Buhrman R A 2005 *Appl. Phys. Lett.* **86** 152509
[19] Hayakawa J, Ikeda S, Lee Y M, Sasaki R, Meguro T, Matsukura F, Takashi H and Ohno H 2005 *Japan. J. Appl. Phys.* **44** L1267
[20] Slonczewski J C 2002 *J. Magn. Magn. Mater.* **247** 324
[21] Slonczewski J C 2005 *Phys. Rev.* B **71** 024411
[22] Stiles M D and Zangwill A 2002 *Phys. Rev.* B **66** 014407
[23] Barnas J, Fert A, Gmitra M, Weymann I and Dugaev V K 2005 *Phys. Rev.* B **72** 024426
[24] Zhang S, Levy P M and Fert A 2002 *Phys. Rev. Lett.* **88** 236601
[25] Slavin A and Tiberkevich V 2005 *Phys. Rev. Lett.* **95** 237201
Slavin A N and Tiberkevich V S 2005 *Phys. Rev.* B **72** 094428
[26] Edwards D M, Federici F, Mathon J and Umerski A 2005 *Phys. Rev.* B **71** 054407
[27] Heide C 2001 *Phys. Rev.* B **65** 054401
[28] Tserkovnyak Y, Brataas A, Bauer G E W and Halperin B I 2005 *Rev. Mod. Phys.* **77** 1375
Heinrich B, Tserkovnyak Y, Woltersdorf G, Brataas A, Urban R and Bauer G E W 2003 *Phys. Rev. Lett.* **90** 187601
[29] Lee K J, Deac A, Redon O, Noziéres J P and Dieny B 2004 *Nat. Mater.* **3** 877
[30] Stiles M D and Miltat J 2006 Spin transfer torque and dynamics *Dynamics in Confined Magnetic Structures III: Topics in Applied Physics 101* ed B Hillebrands and A Thiaville (Berlin: Springer) pp 225–308
[31] Sun Q F and Xie X C 2005 *Phys. Rev.* B **72** 245305
[32] Valet T and Fert A 1993 *Phys. Rev.* B **48** 7099
[33] Zhu Z G, Su G, Jin B and Zheng Q R 2003 *Phys. Lett.* A **306** 249
Zhu Z G, Su G, Zheng Q R and Jin B 2003 *Phys. Rev.* B **68** 224413
[34] Xiao J, Zangwill A and Stiles M D 2004 *Phys. Rev.* B **70** 172405
[35] Slonczewski J C 2004 *J. Magn. Magn. Mater.* **272** e1465
[36] Manchon A and Slonczewski J C 2006 *Phys. Rev.* B **73** 184419
[37] Tulapurkar A, Suzuki Y, Fukushima A, Kubota H, Maehara H, Tsunekawa K, Djayaprawira D D, Watanabe N and Yuasa S 2005 *Nature* **438** 339
[38] Nunez A S, Duine R A and MacDonald A H 2005 *Preprint* cond-mat/0510797
[39] Shpiro A, Levy P and Zhang S 2003 *Phys. Rev.* B **67** 104430
[40] Manchon A, Strelkov N, Deac A, Vedyayev A and Dieny B 2006 *Phys. Rev.* B **73** 184418
[41] Strelkov N, Vedyayev A and Dieny B 2003 *J. Appl. Phys.* **94** 3278
[42] Fert A *et al* 2004 *J. Magn. Magn. Mater.* **272** 1706
[43] Julliére M 1975 *Phys. Lett.* A **54** 225
[44] Ideka S, Hayakawa J, Lee Y M, Sasaki R, Meguro T, Matsukura F and Ohno H J 2005 *J. Appl. Phys.* **44** L1442
Yuasa S, Fukushima A, Kubota H, Suzuki Y and Ando K 2006 *Appl. Phys. Lett.* **89** 042505
[45] Mathon J 1997 *Phys. Rev.* B **56** 11810
[46] Butler W H, Zhang X G, Schulthess T C and MacLaren J M 2001 *Phys. Rev.* B **63** 054416
[47] Belashchenko K D, Velev J and Tsymbal E Y 2005 *Phys. Rev.* B **72** 140404
[48] Tsymbal E Y and Pettifor D G 2001 *Phys. Rev.* B **64** 212401
Tsymbal E Y, Sokolov A, Sabirianov I F and Doudin B 2003 *Phys. Rev. Lett.* **90** 186602
[49] Zhuravlev M Y, Tsymbal E Y and Vedyayev A V 2005 *Phys. Rev. Lett.* **94** 026806
[50] Vedyayev A, Bagrets D, Bagrets A and Dieny B 2001 *Phys. Rev.* B **63** 064429
[51] Kalitsov A, Theodonis I, Kioussis N, Chshiev M, Butler W H and Vedyayev A 2006 *J. Appl. Phys.* **99** 08G501

[52] Keldysh L V 1965 *Sov. Phys.—JETP* **20** 1018
[53] Rammer J and Smith H 1986 *Rev. Mod. Phys.* **2** 323
[54] Bratkovsky A M 1997 *Phys. Rev.* B **56** 2344
[55] Li F F, Li Z Z, Xiao M W, Du J, Xu W and Hu A 2004 *Phys. Rev.* B **69** 054410
[56] Sharma M, Wang S X and Nickel J H 1999 *Phys. Rev. Lett.* **82** 616
[57] Manchon A, Ryzhanova N, Strelkov N, Vedyayev A and Dieny B 2006 *J. Magn. Magn. Mater.* at press
[58] Rudzinski W, Swirkowicz R, Barnas J and Wikzynski M 2004 *J. Magn. Magn. Mater.* **294** 11–9
[59] Berger L 2003 *J. Appl. Phys.* **93** 7693
[60] Urazhdin S, Birge N O, Pratt W P and Bass J 2004 *Appl. Phys. Lett.* **84** 1516
Urazhdin S, Kurt H, AlHajDarwish M, Birge N O, Pratt W P Jr and Bass J 2005 *J. Appl. Phys.* **97** 10C701
[61] Tsoi M 2006 private communication
[62] Pratt W P 2005 private communication
[63] Theodonis I, Kioussis N, Kalitsov A, Chshiev M and Butler W H 2006 *Phys. Rev. Lett.* **97** 237205
[64] Levy P M and Fert A 2006 *Phys. Rev. Lett.* **97** 097205